**Technische Universität Berlin**
Fakultät II - Mathematik und Naturwissenschaften
Institut für Optik und Atomare Physik

# Characterizing Spintronic Materials by Terahertz Spectroscopy

## Master Thesis

by Oliver Philipp Gückstock

This work was done at the
**Fritz-Haber-Institute of the Max-Planck-Society**
Terahertz Physics Group
Prof. Dr. Tobias Kampfrath

**Primary supervisor:** Prof. Dr. Stefan Eisebitt (TU Berlin)
**Secondary supervisor:** Prof. Dr. Martin Wolf (FHI Berlin)

Berlin, Februar 2018

# Eidesstattliche Erklärung

*Hiermit erkläre ich, dass ich die vorliegende Arbeit selbstständig und eigenhändig sowie ohne unerlaubte fremde Hilfe und ausschließlich unter Verwendung der aufgeführten Quellen und Hilfsmittel angefertigt habe.*
*Die selbstständige und eigenständige Anfertigung versichere ich an Eides statt:*

Berlin, den

..............................................................................................................
Unterschrift

# Abstract

State-of-the-art electronic devices for information processing are to the largest extend based on the transport and storage of electron charges. The field of spintronics might be a possible future trend toward more energy efficient and much faster operating systems. In spintronics, the orbital magnetic moment of an electron, the spin, is used as information carrier instead of the electron charge. A central operation for the integration into conventional electronics is the conversion of charge currents into spin currents and vice versa. The (inverse) spin Hall effect describes this conversion process and plays, thus, a central role for the generation and detection of spin currents.

Conventional electronics already reached operation speeds which exceeds the gigahertz regime. Thus, spin-based concepts could also be transferred to the terahertz (THz) range. Therefore, the motivation of combining the two fields of spintronics and THz spectroscopy is given naturally. So, there is a need to maximize the spin-to-charge conversion efficiency at highest frequencies.

In this work, we study promising material systems that have a high potential to be employed in spintronic devices. Sample structures, such as thin film bilayers consisting of a ferromagnet (FM) and a non-magnetic layer (NM), are in the focus of this thesis' research with regard to their spin-orbit-coupling properties. To reveal internal spin Hall parameters of the NM layer at high frequencies straightforwardly, THz emission spectroscopy is shown to be a suitable tool. Importantly, the THz emission technique is an all-optical, contact-free method that requires no micro-structuring compared to common electrical spin-Hall-effect measurement schemes. Thereby it offers the possibility to rapidly measure many samples as e.g. binary alloys over their complete concentration range. In this thesis, two different binary alloys are studied: tantalum-gold and gold-platinum, measured over their complete concentration range, as well as a promising phase of tungsten, doped with varying oxygen concentrations.

Finally, this thesis briefly shows the development of an electromagnet that generates a rotating magnetic field. A potential application is the modulation of the THz polarization emitted from optically excited FM|NM layers. The basic idea and the first prototype are presented. The prototype is tested in the dc mode while measuring magnetic hysteresis loops of thin-film FM|NM bilayers by THz emission spectroscopy. In the ac mode, a first test with rotating magnetic fields is shown in the outlook.

# Kurzfassung

Die heutzutage genutzte Elektronik in der Informationsverarbeitung basiert weitestgehend auf dem Transport und der Speicherung von elektrischen Ladungen. Eine mögliche Weiterentwicklung zu energetisch effizienteren und schnellen Systemen stellt die sogenannte Spintronik dar. Hierbei wird anstatt der Ladung eines Elektrons, sein aus dem Bahndrehimpuls resultierendes magnetisches Moment, der Spin, genutzt. Eine der wichtigsten Grundoperationen bei der Integration des Spins in ladungsbasierte Elektronik, stellt die Umwandlung eines Ladungstromes in einen Spinstrom und umgekehrt dar. Der (inverse) Spin Hall Effekt beschreibt genau solche Umwandlungsprozesse und spielt somit eine zentrale Rolle im Bereich von Spinströmen.

Konventionelle Elektronik ist bereits heute in der Lage bei Geschwindigkeiten jenseits des Gigahertz-Regimes zu arbeiten. Spin-basierte Konzepte könnten demnach ebenfalls im Terahertz (THz) Bereich einzusetzen zu sein. Somit lässt sich die Verbindung der Forschungsfelder der Spintronik und THz Spektroskopie auf einfachste Weise motivieren. Es gibt demnach einen Bedarf die Effizienz der Spin-zu-Ladungskonversion bei hohen Frequenzen zu maximieren.

In dieser Arbeit untersuchen wir vielversprechende Materialien, welche potentiell in spintronischen Bauelementen genutzt werden könnten. Es werden Probenserien dünner Bilagen, bestehend aus einem Ferromagneten (FM) und nicht-magnetischen Metallen (NM), hinsichtlich ihrer Spin-Bahn-Kopplungseigenschaften untersucht. Um direkten Zugriff auf die internen Spin Hall Parameter der NM-Schicht bei hohen Messfrequenzen zu erlangen, setzen wir THz Emissionsspektroskopie als Messmethode ein. Die THz Emissionsspektroskopie bietet als optische Messtechnik im Gegensatz zu herkömmlichen, elektrischen Methoden zur Messung des Spin Hall Effekts, die Vorteile kontaktfrei und frei von der Notwendigkeit einer Mikrostrukturierung zu sein. Dadurch ergibt sich die Möglichkeit komplexere Materialien, wie binäre Legierungen, über den gesamten Kompositionsbereich entsprechend vieler Proben, sehr zügig zu untersuchen. Es werden drei Materialsysteme in dieser Arbeit untersucht: zwei binäre Legierungen, Tantal-Gold und Gold-Platin, gemessen über den gesamten relativen Konzentrationbereich, sowie eine vielversprechende Phase des Metalls Wolfram, welches mit variierender Sauerstoffkonzentration dotiert wird.

Abschließend wird die Entwicklung eines Elektromagneten präsentiert, welcher ein rotierendes Magnetfeld erzeugt. Eine potentielle Anwendung ist die Möglichkeit zur Modulation der THz Polariation von optisch angeregten FM|NM Schichten. Es wird die Grundidee und ein erster Prototyp vorgestellt. Die Funktion des Prototyps wird im DC-Modus durch THz Emissionsmessungen von magnetischen Hysteresen an FM|NM-Bilagen demonstriert. Ein erster Test mit rotierendem Magnetfeld im AC-Modus wird als Ausblick gezeigt.

# Contents

# 1. Introduction

This thesis deals with spintronic effects at THz frequencies. It is, therfore, at the interface of two research fields, spintronics and THz spectroscopy, which are briefly introduced in the following.

## 1.1. Spin currents and spin-to-charge conversion

Most of the digital data worldwide is stored as magnetic bits, for instance, in big server farms of the information technology global players. Data transport requires a conversion from magnetic to electronic information [Cha07]. The latter is represented as a charge current in conventional electronics. One idea to overcome this need for conversion is the idea to transport magnetic information directly. This new approach could support conventional electronics by making use of the intrinsic angular momentum (spin) of the electron [Wol01], which is accompanied by a magnetic moment. The goal of these spin-based electronics field, called "spintronics" is to use the electron spin as an information carrier and transport spin information via spin currents [Sve15]. This requires the fundamental operations of efficient generation and detection of spin currents. For this purpose, suitable spintronic effects such as the spin-dependent Seebeck effect (SDSE), the (inverse) spin Hall effect (SHE) and spin Seebeck effect (SSE) are exploited [Uch08, Bau12, Sin15].

The generation of spin currents can be realized by several concepts. Briefly, spin currents can be generated by electric fields in magnetic metals [Sch05]. Alternatively spin currents can be driven by temperature gradients in magnetic conducting or insulating materials [Ong08]. Spin pumping by precessional motion of the magnetization and subsequent interaction with spins in a non-magnetic layer, represents the third possibility [Uch12].
The integration of spin currents into conventional charge-based electronics requires the conversion from spin currents into charge currents and backwards [Wol01]. The most popular effect is the spin Hall effect.

The goal is to implement all these effects and basic operations into conventional electronics at the highest possible operation speeds. To become comparable and to go beyond the speed of present electronic devices, we are reaching the terahertz (THz) frequency range [Bra16a]. A question that arises in this context is whether central spintronic effects, e.g. SDSE or SHE are still operative at THz frequencies [Kam13a]. Finally, this requires new and efficient materials. In particular, materials with a high spin-orbit-coupling (SOC) have the potential to be efficient for spintronic applications.
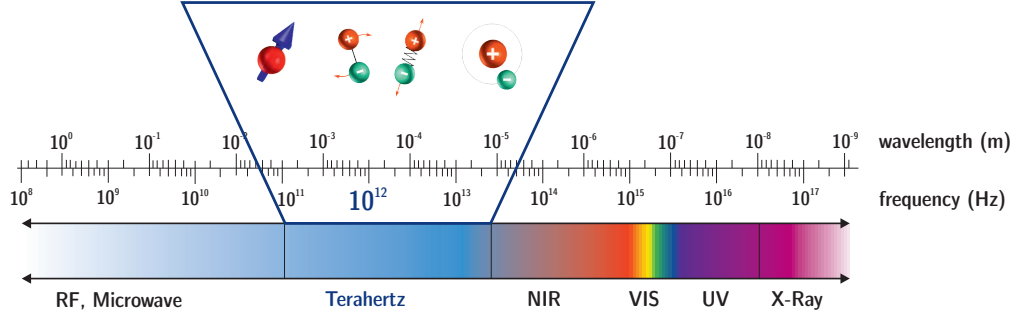
**Figure 1.1.: Terahertz window.** The terahertz regime is located between the near-infrared (NIR) and the microwave range and lies roughly between 0.3 and 30 THz. The THz photon energy coincides with many fundamental modes, e.g. the precession of spins, rotation of molecules, lattice vibrations or bound electron-hole states (excitons). Figure redrawn from [Sei13].

## 1.2. Terahertz spectroscopy

The THz window of the electromagnetic spectrum comprises electromagnetic radiation with frequencies between 0.3 - 30 THz. This regime, schematically shown on Fig. 1.1, bridges microwave-based electronics and laser-based photonics [Brü12].

Terahertz radiation has the advantage that it can couple resonantly to many fundamental modes such as magnons and phonons in solids or to vibrational and rotational modes of molecules [Saj17] in gases and liquids. Furthermore, spin-orbit-interaction energies are often in the THz regime [Wal16] and binding energies of excitons and cooper pairs coincide with the scale of the THz photon energy ($1\,\mathrm{THz} \,\hat{=}\, 4\,\mathrm{meV}$) [Hwa15].

THz time-domain spectroscopy provides access to all these fundamental modes. In addition, by measuring the terahertz electric field as a function of time with a suitable detection method, one can obtain amplitude and phase information simultaneously [Sei17c]. A need for THz sources arises, which combines ideally characteristics such as to be efficient, cheap, broadband, scalable, and suitable for high power systems [Dhi17].

Recent works used terahertz spectroscopy to reveal processes where spintronics plays a major role in conducting and semiconducting solids [Jin15, Hui17, Pri15]. One method to study ultrafast spin and charge dynamics with THz radiation is THz emission spectroscopy [Lei99, Kam13a].

## 1.3. This thesis

In this thesis, the major topic is the characterization of spintronic materials for efficient spin-to-charge conversion by terahertz spectroscopy. For this purpose, we study THz emission and extract spin Hall related parameters such as the spin Hall angle or

the spin relaxation length.

Until now, mostly pure materials were studied, e.g to build new THz emitters. By taking advantage of the terahertz emission method to screen very fast and contact-free complex compounds, we extend our studies to binary material systems. We focus on experiments of spin-to-charge conversion in binary alloys and doped systems in this thesis. In particular, three different materials are studied: a gold-platinum alloy, a tantalum-gold alloy and oxygen-doped $\beta$-tungsten.

In the second part of this thesis, we demonstrate an electromagnet for fast switching/rotating of the in-plane magnetization in thin-film samples. This modulation of the magnetization aims at increasing the signal-to-noise ratio for magnetization-sensitive measurements in the future. Here, the first prototype is used to measure magnetic hysteresis loops of thin bilayers in the dc mode. Moreover, we show a first proof of operation in the ac mode and modulate of the in-plane magnetization of a thin-film sample.

# 2. Theoretical background

This chapter provides the necessary theoretical background to understand the experimental concepts and results in this thesis. Basic information on the electron spin, magnetic ordering in solids, spin currents and the generation of those are given in the following. Furthermore, the theory of the spin Hall effect and methods to measure this spintronic-relevant effect in different frequency ranges is presented.

## 2.1. The electron spin

The Schrödinger equation is one of the basic equations in quantum mechanics. It describes the time-evolution of a quantum mechanical system in the non-relativistic limit. This equation is not sufficient to describe the full spectrum of magnetic effects, because it neglects the spin of the electron [Nol15]. The Dirac equation is the relativistic variant of the Schrödinger equation and includes the electron spin $\hat{\boldsymbol{s}}$, which is an intrinsic angular momentum. So, electrons exhibits two types of angular momentum: orbital $\hbar\hat{\boldsymbol{l}}$ and intrinsic $\hbar\hat{\boldsymbol{s}}$. The spin is linked to a magnetic moment $\hat{\boldsymbol{\mu}}_{\mathrm{s}}$, which is given by

$$\hat{\boldsymbol{\mu}}_{\mathrm{s}} = -g_{\mathrm{e}}\mu_{\mathrm{B}}\hat{\boldsymbol{s}} \tag{2.1.1}$$

with the g-factor for electrons $g_{\mathrm{e}}$, the Bohr magneton $\mu_{\mathrm{B}}$ and the reduced Planck constant $\hbar$ [Nol15]. Analogous to the two contributions to the total angular momentum of an electron, the total electron magnetic moment $\hat{\boldsymbol{\mu}}_{\mathrm{e}}$ is given by

$$\hat{\boldsymbol{\mu}}_{\mathrm{e}} = \hat{\boldsymbol{\mu}}_{\mathrm{s}} + \hat{\boldsymbol{\mu}}_{\mathrm{l}}. \tag{2.1.2}$$

Hereinafter, we denote vectors with bold symbols, commutators with a hat over the symbol and tensors are depicted by an underline.

## 2.2. Magnetic order in solids

The Pauli exclusion principle states that two fermions such as electrons have to differ in at least one quantum number. We illustrate this statement for a two-electron model system described by their wavefunction $\Psi(\boldsymbol{r}_1, \boldsymbol{s}_1, \boldsymbol{r}_2, \boldsymbol{s}_2)$. We factorize the wavefunctions into an orbital part and a spin part [Nol15]. Since electrons are fermions, the total wavefunction has to be antisymmetric by exchanging $1 \Leftrightarrow 2$. With this boundary condition, one can construct four product wavefunctions with either symmetric or antisymmetric orbital and spin parts. There are a singlet state which has a total

spin of $S = 0$ and three triplet states with $S = \hbar$. They are defined as

$$|\Psi_{\text{singlet}}\rangle = |\Phi_{\text{s}}\rangle \left( |\uparrow, \downarrow\rangle - |\downarrow, \uparrow\rangle \right) / \sqrt{2} \tag{2.2.1}$$

$$|\Psi_{\text{triplet}}\rangle = |\Phi_{\text{as}}\rangle \begin{cases} |\uparrow, \uparrow\rangle \\ \left( |\uparrow, \downarrow\rangle + |\downarrow, \uparrow\rangle \right) / \sqrt{2} \\ |\downarrow, \downarrow\rangle \end{cases} \tag{2.2.2}$$

The triplet state, which describes parallel alignment of the two electron spins, is energetically preferred by the system in the majority of cases taking the Coulomb interaction between the electrons into account [Whi72]. In summary, a spontaneous spin ordering can be caused by the combination of Pauli's exclusion principle and the Coulomb interaction of the electrons. This interaction can be expressed as an effective spin-spin interaction by an isotropic exchange-interaction Hamiltonian

$$\hat{H}_{\text{exch}} = \text{const.} - \frac{1}{4} J_{\text{exch}} \hat{\boldsymbol{s}}_1 \cdot \hat{\boldsymbol{s}}_2 / \hbar^2 \tag{2.2.3}$$

with $J_{\text{exch}} = E_{\text{singlet}} - E_{\text{triplet}}$ representing the exchange constant.

We will show one simple model to describe magnetic ordering: the Stoner model which considers magnetic moments as delocalized electrons [Sto06]. The basic assumption of the model is an energy separation of the band structure for spin-up and spin-down electrons. An energy splitting of the two spin channels can be preferred by the system depending on the density of states at the Fermi energy and on the strength of the exchange interaction [Nol15]. This results in an asymmetry in the population of majority and minority electrons. In total, a spin order is achieved which causes in a net magnetization. Macroscopically spontaneous ordering of the magnetic moments $\boldsymbol{\mu}_i$ sums up to the magnetization $\boldsymbol{M}$ of the solid with volume $V$

$$\boldsymbol{M} = \frac{1}{V} \sum_i \boldsymbol{\mu}_i. \tag{2.2.4}$$

## 2.3. Magnetic anisotropy and hysteresis

The above introduced exchange interaction is isotropic. However, also anisotropic spin-dependent contributions to the total energy of the system can arise from spin-orbit interaction and spin-spin magnetic dipole interaction. The magnetization then favors one of the directions (e.g. "easy axis") in the solid which show a minimum in the anisotropy energy [Sto06].
This anisotropy becomes e.g. apparent in magnetic hysteresis loops which describe the response of a magnetic material to an external magnetic field [Sto06]. However, this response is not linear. By applying the external magnetic field $\mathbf{B}_{\text{ext}}$ a torque $\mathbf{T}$ will act on the magnetization

$$\boldsymbol{T} = \boldsymbol{M} \times \boldsymbol{B}_{\text{ext}}. \tag{2.3.1}$$
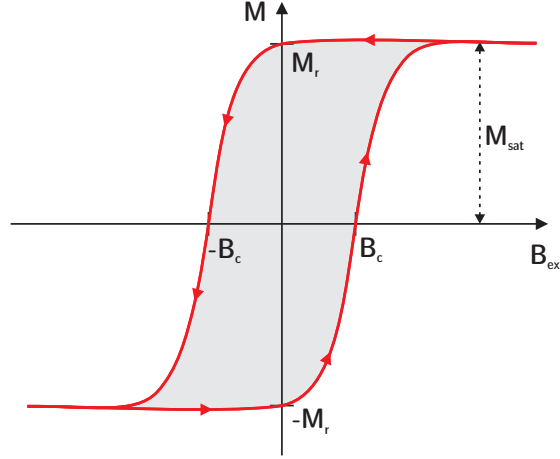
**Figure 2.1.: Magnetic hysteresis loop**. The magnetization of a ferromagnetic medium shows a non-linear response to an applied external magnetic field. To switch from one magnetization state to the opposite, a minimum field, called the coercive field $B_c$, is needed. The maximum reachable magnetization $M_{sat}$ and remanence magnetization $M_r$ are also shown.

The magnetization follows the external field to minimize its energy [Sto06]. In the simplest case, the ferromagnet has only one single easy axis. One can consider two contributions in terms of energy:

$$E = E_a + E_m = K_u \sin^2\theta + B_{ext}M_{sat}\cos(\phi - \theta) \qquad (2.3.2)$$

where $E_a$ is the anisotropy energy and $E_m$ represents the magnetostatic energy. For materials with an easy axis perpendicular to the hard axis, the anisotropy energy is only dependent on the angle $\theta$ between magnetization and the easy axis and on the anisotropy constant $K_u$ which is a material parameter. The magnetostatic energy depends on the the saturation magnetization $M_{sat}$, the external magnetic field, $\theta$ and an angle $\phi$ between $B_{ext}$ and the easy axis. By minimizing the total energy of this simple model system, one can find two solutions for the magnetization. The first is called "hard axis" where the magnetization goes linearly with $B_{ext}$ up to $M_{sat}$ and reads

$$M = M_{sat}\frac{B_a}{B_{ext}} \qquad (2.3.3)$$

with the anisotropy field $B_a$. The second solution is the "easy axis" which has a rectangular shape in the ideal case. In the easy axis, the energy of the system is minimized between

$$-\frac{2K_u}{M_{sat}} < B_{ext} < \frac{2K_u}{M_{sat}}. \qquad (2.3.4)$$

In summary, there are different shapes of hysteresis loops possible, depending on the initial state of the magnetic moments and on the material properties. One characteristic shape is shown in Fig. 2.1. At least parallel to the external field, it is possible to reduce the net magnetization of a ferromagnetic material to zero. The required magnetic field is called coercive field $B_c$. When all magnetic moments are aligned parallel

to the external field, we reach the saturation magnetization $M_{\text{sat}}$. In ferromagnets, external fields allow one to align the magnetic moments along the field direction. If we switch off the external field, the remaining magnetization is called remanence.

## 2.4. Charge and spin currents

In this thesis, both charge ans spin transport by electrons are studied. Therefore, the concepts of charge and spin currents are briefly outlined in the following.

### a) Charge currents
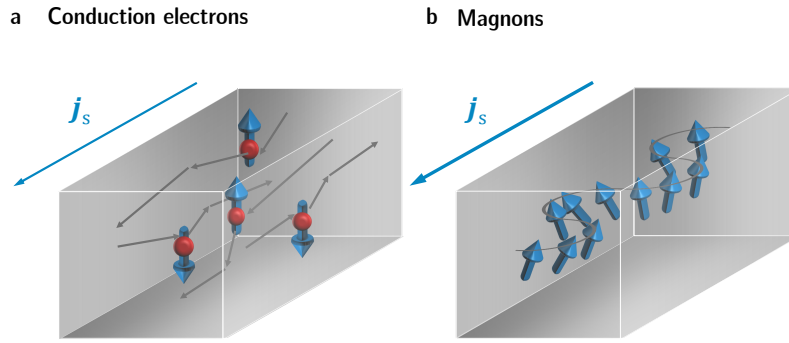


Figure 2.2.: **Spin currents.** **a**, Spin currents which transport spin by conduction electrons. **b**, Magnon spin current. Figure created with the help of T. Seifert and redrawn from [Kaj10].

To describe the transport of conduction electrons, use the classical continuity equation [Dem13]

$$\frac{\partial}{\partial t}\rho + \boldsymbol{\nabla}\boldsymbol{j}_{\text{c}} = 0 \tag{2.4.1}$$

where $\boldsymbol{j}_{\text{c}}$ is the charge current and $\rho$ is the density of charges in a specific volume. Equation 2.4.1 describes that a number of charges per volume can change by a flow, e.g. a charge current, which has a certain direction and is formalized as a vector. Conduction electrons show a diffusive propagation and such charge currents are carried by electrons (Fig. 2.2a). To describe electrical conduction in a simple way, a model, established by Paul Drude, is often employed in today's work. Hereby, the basic assumption is, that conduction electrons can move relative freely through the metal, whose velocity scales with time constant $\tau$ [Ash76]. $\tau$ can be interpreted as the time between subsequent elastic collisions of conduction electrons. In total we yield [Ash76]

$$\sigma_{\text{Drude}} = \frac{\sigma_{\text{dc}}}{1 + i\omega\tau} \qquad \text{with} \qquad \sigma_{\text{dc}} = \frac{ne^2\tau}{m} \tag{2.4.2}$$

with angular velocity $\omega$, electron mass $m$, number of electrons $n$ and electron charge $e$.

**b) Spin currents**

There are two different concepts to generate spin currents which transport information through space: by the flow of spin-polarized (conduction) electrons or by magnons. The latter describes a collective precession of spins that moves like a wave through space (spin waves). Spin currents $\boldsymbol{j}_{\mathrm{s}}$ are described as a tensor of 2nd rank, which captures the propagation direction and spin-polarization of the current. The latter is proportional to the tensor product of the linear velocity $\boldsymbol{v}$ and the magnetization $\boldsymbol{M}$. Two different sorts of spin currents may arise. First, spin-polarized charge current: an unbalanced amount of the two spin species in the medium results in a spin-polarized charge current due to the fact that spin-up and spin-down electrons have an opposite spin polarization. Second, a pure spin current carried by a collective precession of spins, e.g in magnetic insulating materials. A wave-like transport of angular momentum is generated, whose quasi-particle is called magnon (Fig. 2.2b). A continuity equation for spin currents can be written as [Sun05]

$$\frac{\mathrm{d}}{\mathrm{d}t}\boldsymbol{M} + \boldsymbol{\nabla} \cdot (\boldsymbol{v} \otimes \boldsymbol{M}) = -\boldsymbol{\omega} \times \boldsymbol{M} \qquad (2.4.3)$$

with the linear velocity $\boldsymbol{v}$ and the angular frequency $\boldsymbol{\omega}$. According to Sun *et al.*, we define a linear current density $\underline{\boldsymbol{j}}_{\mathrm{s}} := \boldsymbol{v} \otimes \boldsymbol{M}$ and an angular current density $\boldsymbol{j}_{\omega} := \boldsymbol{\omega} \times \boldsymbol{M}$ [Sun05]. Importantly, an additional parameter to describe the spin-current transport is considered: a torque can act on the spin which leads to precession around its equilibrium state. In total, this yields an equation in the non-relativistic limit [An12] which reminds us of the continuity equation for charges (see Eq. 2.4.1)

$$\frac{\mathrm{d}}{\mathrm{d}t}\boldsymbol{M} + \boldsymbol{\nabla} \cdot \underline{\boldsymbol{j}}_{\mathrm{s}} = \boldsymbol{j}_{\omega} \qquad (2.4.4)$$

with a spin transport term $\boldsymbol{\nabla} \cdot \underline{\boldsymbol{j}}_{\mathrm{s}}$ and a spin torque term $\boldsymbol{j}_{\omega}$.

## 2.4.1. Generation of spin currents

Flow of spin angular momentum can happen by transport of spin-polarized electrons and/or simply by torque, e.g. spin pumping and magnons. The generalized definition of spin current is "the flow of spin angular momentum". The generation of spin currents is an important and elementary spintronic operation. In the following, three different methods will be presented to create spin currents based on electrical and temperature gradients in conducting and even insulating magnets, and based on the spin pumping effect.

**1) Electric fields in magnetic metals**

The generation of spin-polarized electron currents in magnetic metals is relatively straightforward. By applying an electric field to a ferromagnet, a current flows inside the magnet. Due to the different conductivities of majority and minority spin
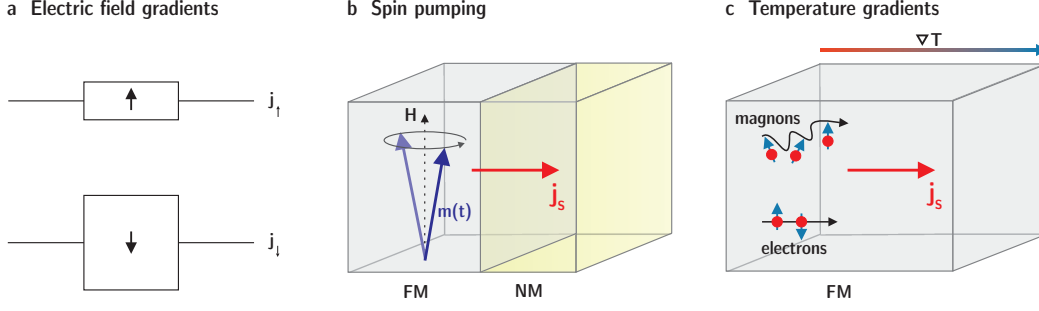
**a** Electric field gradients   **b** Spin pumping   **c** Temperature gradients

Figure 2.3.: **Generation of spin currents. a**, By electric field gradients in ferromagnetic materials a charge current arises. Due to different conductivities for majority and minority charges (box sizes), the current gets spin-polarized. **b**, Spin pumping: Magnetization precesses around its equilibrium state. The damping of this precession leads to the emission of a spin curent into the NM layer. **c**, A temperature gradient creates a spin current which is carried by magnons in magnetic insulating materials or by electrons in magnetic conductors. Fig. **b** is redrawn from [Wei14] and **c** is redrawn from [Uch12].

electrons inside the FM, the generated longitudinal current is spin-polarized (Fig. 2.3a). To illustrate the generated spin current, we use a two-current model, where the contributions of spin-up ($\uparrow$) and spin-down ($\downarrow$) electrons read

$$\boldsymbol{j}_\uparrow \;=\; \sigma_\uparrow \boldsymbol{E} \tag{2.4.5}$$

$$\boldsymbol{j}_\downarrow \;=\; \sigma_\downarrow \boldsymbol{E} \tag{2.4.6}$$

In the case of an unbalanced amount of spin-up and spin-down electrons, we yield a net spin current:

$$\boldsymbol{j}_\uparrow - \boldsymbol{j}_\downarrow = \left(\sigma_\uparrow - \sigma_\downarrow\right)\boldsymbol{E}. \tag{2.4.7}$$

The total spin current $\boldsymbol{j}_\mathrm{s}$ is proportional to $\boldsymbol{M} \otimes \left(\boldsymbol{j}_\uparrow - \boldsymbol{j}_\downarrow\right)$.

For the integration of such spin currents into classical semiconductor-based electronics, the goal is to inject this spin current from a ferromagnetic metal into a semiconductor. However, due to much higher resistances of the conduction electrons in the semiconductor compared to which are present in the magnet, combining these concepts is challenging. To overcome the resistance mismatch, insulating intermediate layers such as MgO are used through which electrons tunnel into the semiconductor [Sch05]. This intermediate layer also acts as a spin filter.

## 2) Spin pumping

As discussed above, spin currents are also possible by spin torques, e.g. at interfaces. A concept that uses this spin torque to generate a spin current, is spin pumping. It describes the process when an external magnetic field at radio frequencies is coupled to a ferromagnetic layer and creates a spin current in the NM layer. The magnetization of the FM layer starts precessing around its equilibrium state if the frequency of the magnetic field is close to the ferromagnetic resonance frequency (see Fig. 2.3b). The magnetization precession including Gilbert damping $\alpha$ and spin-exchange interaction

$J_{\text{ex}}$ can be written as follows

$$\frac{\mathrm{d}\boldsymbol{M}}{\mathrm{d}t} = \boldsymbol{M} \times \boldsymbol{B}_0 + \alpha\boldsymbol{M} \times \frac{\mathrm{d}\boldsymbol{M}}{\mathrm{d}t} + \boldsymbol{M} \times J_{\text{ex}}\boldsymbol{m}_N \qquad (2.4.8)$$

where $\mathbf{m}_N$ is the induced magnetization in the NM layer [Xu16].

Damping happens due to the coupling of the precessing magnetization to other degrees of freedom. The NM layer located next to the FM layer contains conduction electrons whose spin interacts via spin-exchange interaction $J_{\text{ex}}$ with the magnetization in the FM layer [Xu16]. This interaction induces a transfer of angular momentum to the spins in the NM layer. Spins in the NM layer, located close to the FM/NM interface, become polarized. Due to a spin-polarization gradient, a spin current arises.

### 3) Temperature gradients in magnets

Temperature gradients in magnets are able to generate spin currents. They are named after the classical Seebeck effect, where a voltage is generated by placing a conductor in a temperature gradient [Uch08]. Two possible scenarios with different underlying physics are conceivable [Bau12]. First, the spin-dependent Seebeck effect is dominant in ferromagnetic conductors. Second, the spin Seebeck effect works mostly in ferromagnetic insulator [Wu16]. Both scenarios are depicted in Fig. 2.3c.

### 3a) Spin-dependent Seebeck effect

To a certain extend, this situation is an analogon to section 2.4.1 with $\boldsymbol{E}$ replaced by $\boldsymbol{\nabla}T$. By heating a ferromagnet, a temperature gradient is formed across the structure. The classical Seebeck effect creates a charge current inside the ferromagnet [Bau12]. Majority and minority electron spins have different Seebeck coefficients $S_{\uparrow/\downarrow}$ which read similarly according to the two-current model introduced in section 2.4.1:

$$\boldsymbol{j}_\uparrow \quad \propto \quad S_\uparrow \boldsymbol{\nabla}T \qquad (2.4.9)$$

$$\boldsymbol{j}_\downarrow \quad \propto \quad S_\downarrow \boldsymbol{\nabla}T \qquad (2.4.10)$$

In total, this results in a spin-polarized charge current $\boldsymbol{j}_{\text{s}} \propto \boldsymbol{M} \otimes [(S_\uparrow - S_\downarrow)\boldsymbol{\nabla}T]$.

### 3b) Spin Seebeck effect

The classical bulk spin Seebeck effect is also driven by a temperature gradient, but operates dominantely in magnetic insulators. A prototypical system is e.g. yittrium-iron-garnet (YIG) [Sei17b]. Here, magnons are responsible for the spin current due to the negligible contribution of the conduction electrons [Bau12]. We have to note that the spin Seebeck effect can also be present in magnetic conductors, but its contribution is small compared to the spin-dependent Seebeck effect.

Recently, an exciting effect was discovered: the spin Hall effect. It generates transverse spin currents without external magnetic fields, by only applying an electric field.
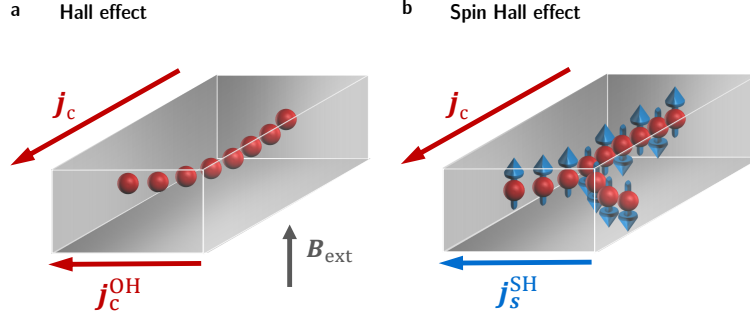
## 2.5. Spin Hall effect (SHE)



**Figure 2.4.: Hall effects. a,** Schematic picture of the ordinary Hall effect (OHE), which describes the transformation of a charge current $j_c$ into a transverse charge current $j_c^{OH}$ due to a transverse applied external magnetic field $B_{ext}$ in an electrical conductor. **b,** Spin Hall effect: the applied charge current $j_c$ is converted into a transverse spin current $j_s^{SH}$. Figure created with the help of T. Seifert and redrawn from [Cha16].

The spin Hall effect is an essential effect in the field of spintronics and describes a charge-to-spin conversion. The spin in a closed system is not conserved [Sin15]. The SHE is also present in non-magnets, which is interesting for spintronic applications. In general, an initial longitudinal charge current induces a transverse transport of spin angular momentum. The conversion efficiency is given by the ratio the spin Hall conductivity $\sigma_{SH}$ and the diagonal conductivity $\sigma_{xx}$, called spin Hall angle $\gamma$. Generally, the spin Hall conductivity $\sigma_{SH}$ is a more fundamental quantity than the spin Hall angle. It is a tensor of third order and defined by

$$j_{s,ij} = \sum_k \sigma_{ijk}^{SH} E_k \qquad (2.5.1)$$

with the electric field $\mathbf{E}$. Three mechanisms can contribute to the spin Hall conductivity [Sin15] which are intrinsic deflection (int), skew scattering (ss), and side-jump scattering (sj):

$$\underline{\sigma}_{SH} = \underline{\sigma}_{int} + \underline{\sigma}_{ss} + \underline{\sigma}_{sj}. \qquad (2.5.2)$$

The dependence on the quasi particle scattering time $\tau$ is a strong indicator for these contributions [Sin15]. The intrinsic deflection and side-jump are independent of $\tau$. In contrast, the Mott-like skew scattering is linearly dependent on $\tau$. One can differentiate straightforwardly between strong and weak disorder in a solid to estimate the relative strengths of the SHE mechanisms. Such experiments have been carried out and could clearly show that there are different dependencies of the spin Hall conductivity on the diagonal conductivity by varying the sample temperature [Miy07].
In the limit of weak disorder, the spin Hall conductivity can be dominated by the

mechanism that scales with the quasi particle lifetime. In contrast, for strong disorder, however, intrinsic deflection and side-jump scattering dominate the spin Hall conductivity. The material parameters are crucial for the specific strength of each contribution but Dheer *et al.* showed experimentally that in transition metals, the intrinsic deflection is often larger than the side-jump scattering [Dhe67]. Theoretical calculations by Weischenberg *et al.* support this observation [Wei11].

In contrast, in magnetic metals the anomalous Hall effect (AHE) describes the spin-dependent deflection and is a charge-to-charge conversion, which involves conserved quantities. The AHE can be understood as a SHE of majority and minority electrons, where the unbalanced quantity of majority and minority electrons generates a transverse charge current.

In this thesis, the influence of alloying and doping on the spin Hall conductivity in metallic materials will be measured. Chadova *et al.* [Cha15] pointed out that changes in the lattice parameters, uniaxial strain, etc. result in a dominant intrinsic-contribution change. On the other hand, alloying leads to a predominant manipulation of the extrinsic mechanisms [Lac14, Cha15, Zou16, Lac17, Ram17]. But nevertheless, there are reports on the manipulation of the spin Hall parameters in alloys by dominating intrinsic contributions [Ngu16, Obs16, Che17, Qu18] due to the strong disorder limit. In general, the dominant spin Hall mechanism can vary within the concentration range in alloyed materials [Cra17].

### 2.5.1. Mechanisms

The basic reason for the spin Hall effect in non-magnetic metals is the spin-orbit interaction, which reads

$$\hat{H}_{\mathrm{SOI}} = \frac{\mu_{\mathrm{B}}}{c\hbar}\, \hat{\mathbf{s}} \cdot \left( \frac{\hat{\mathbf{v}}_{\mathrm{e}}}{c} \times \mathbf{E}(\hat{\mathbf{r}}) + \frac{i\hbar}{2cm_{\mathrm{e}}}(\nabla \times \mathbf{E})(\hat{\mathbf{r}}) \right) \qquad (2.5.3)$$

We focus only on the first term as the second one can be usually neglected. To give an intuitive explanation, we ignore that $\hat{\mathbf{s}}$, $\hat{\mathbf{v}}_{\mathrm{e}}$ and $\hat{\mathbf{E}}$ are operators and permute cyclically this triple product:

$$\left( \frac{\hat{\mathbf{v}}_{\mathrm{e}}}{c} \times \hat{\mathbf{E}} \right) \cdot \hat{\mathbf{s}} = \left( \hat{\mathbf{E}} \times \hat{\mathbf{s}} \right) \cdot \frac{\hat{\mathbf{v}}_{\mathrm{e}}}{c} \qquad (2.5.4)$$

By comparing the right hand side of equation 2.5.4 to $\mathbf{A} \cdot \hat{\mathbf{p}}$, it becomes apparent, that $\hat{\mathbf{E}} \times \hat{\mathbf{s}}$ acts like an effective vector potential $\mathbf{A}$ on the electron orbital motion. This is equivalent to an effective magnetic field $\propto (\nabla \times \mathbf{A}) \propto \nabla \times \left( \hat{\mathbf{E}} \times \hat{\mathbf{s}} \right)$. This yields a Lorentz-like force with opposite sign for spin-up and spin-down electrons.
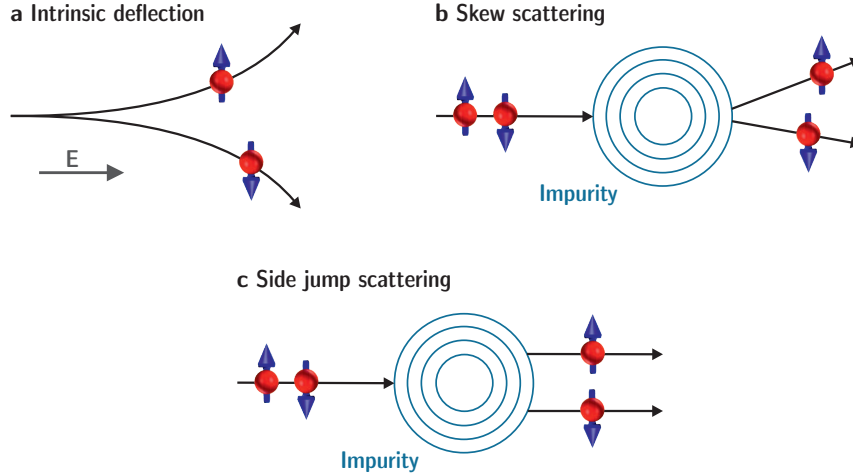
**Figure 2.5.: Scattering mechanisms. a,** Intrinsic deflection: spin-up and spin-down electrons are deflected into opposite directions. **b,** Skew scattering: spins are scattered at an impurity into different directions according to their spin state. **c,** Side jump scattering: electrons experience a lateral displacement at a spherical impurity. Figure redrawn from [Nag10]

## a) Intrinsic deflection

In the intrinsic deflection mechanism no scattering is required because it already originates from a perfect crystal. By studying the intrinsic AHE, Karplus *et al.* [Kar54] observed that electrons, which are traveling through a solid can be influenced by an internal spin-orbit force. This Lorentz-like force leads to a transverse electron velocity (see Fig. 2.5a) [Chu07].

## b) Skew scattering

The skew scattering mechanism may dominate in the small disorder limit and importantly, is proportional to $\tau$. The scattering process leads to a change of the electron wave vector that depends on the spin (see Fig. 2.5b). Skew scattering consists of two fundamental contributions: first, an electron scatters off impurities without spin-orbit coupling by moving in a spin-orbit-coupled band structure and second, electrons scatter off impurities with strong SOC [Sin15].

## c) Side-jump scattering

In contrast to the skew scattering, side-jump scattering is independent of $\tau$. In the modern theoretical framework, it is the remaining part of the total spin Hall conductivity which is not captured by intrinsic deflection and skew scattering. As indicated in Fig. 2.5c, side-jump scattering could be seen as a spin-dependent elastic scattering process by an impurity where the electron keeps its wave vector. In addition, a displacement of the electron in the transverse direction happens which is opposite for opposite spins. Here, the total translational momentum is conserved in contrast to the skew scattering mechanism. Side-jump scattering can be calculated from the

ideal electronic structure of a crystal in the limit of vanishing disorder [Wei11].

## 2.6. Electrical measurement of the SHE

The spin Hall effect is essential for the spin-to-charge conversion. Now, we briefly outline schemes that allow one to measure the SHE by electrical means.

### 2.6.1. Via resonant spin pumping

This method to measure the SHE is based on spin pumping. The sample is magnetized by a static magnetic field $B$. A transverse rf field in the gigahertz range (microwaves) is also applied to the sample using a waveguide to initialize a magnetization precession around the external field (see chapter 2.4.1 part "spin pumping"). If the resonance condition is fulfilled which means that the microwave frequency matches the magnetization precession resonance frequency, called the Larmor frequency, a part of the microwave power is absorbed by the sample. This technique is called ferromagnetic resonance (FMR). The Larmor frequency reads

$$f_{\mathrm{Larmor}} = \frac{\gamma_{\mathrm{e}}}{2\pi} \cdot B \qquad (2.6.1)$$

with the gyromagnetic ratio $\gamma_{\mathrm{e}}$. The partial absorption of microwave power is still working, when the FMR condition is not fulfilled, but the absorption is less efficient. In general, two different modes are conceivable to fulfill the FMR resonance condition. First, by tuning the microwave frequency or second, by sweeping the static magnetic field strength. To detect spin-Hall-effect parameters, a FM|NM structure, mentioned in chapter 2.4.1, is used. By spin pumping a spin current is created, which flows from the FM to the NM layer. The inverse spin Hall effect converts this spin current into a transverse charge current perpendicular to the microwave field direction and the dc magnetic field. Due to e.g. a spin pumping induced loss, the transmitted rf field is affected that is measured as a function of the microwave frequency or the external magnetic field. This technique involves a complex evaluation to get information about the spin Hall parameter.
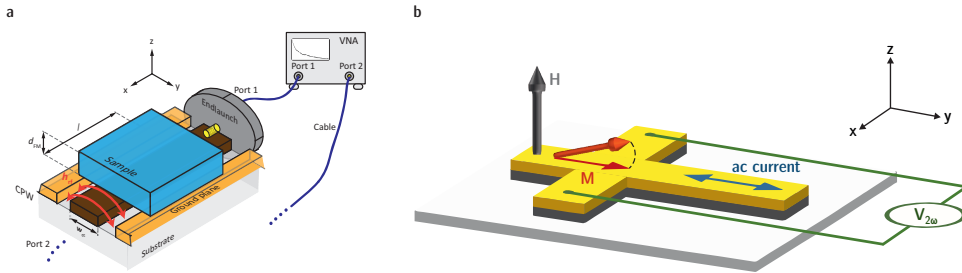


Figure 2.6.: **Resonant spin pumping and harmonic Hall**. **a**, A contact-free, inductive ferromagnetic resonance method using a vector network analyzer (VNA-FMR) is shown. Figure **a** taken from [Lie17] with the permission of L. Liensberger. **b**, Schematic picture of a Hall bar structure for harmonic Hall measurements redrawn from [Hay14].

## 2.6.2. Via the spin Seebeck effect

The spin Seebeck effect can be used to generate spin currents in a non-magnetic layer as described in chapter 2.4.1 part "Spin Seebeck effect". A temperature gradient can be applied by e.g. resistive heating of the sample. By using a FM|NM sample structure, where the FM layer is insulating, e.g. a ferrimagnet like YIG, a spin current across the FM|NM interface due to magnon accumulation in the FM layer, in front of the FM|NM interface is generated. In the NM layer, the inverse spin Hall effect converts the spin current into a transverse charge current. This charge current can be measured electrically by applying contacts.

## 2.6.3. Via harmonic Hall measurements

Samples for harmonic Hall measurements have to be prepared with lithography, because a Hall-bar structure is needed in the NM layer (see Fig. 2.6b). The harmonic Hall technique is based on the following idea. We drive a current in the Hall-bar structure that induces an effective spin-orbit-torque field $H$. If the magnetization is in-plane and parallel to the current, the effective field leads to a slight out-of-plane tilt of the magnetization, pointing to the bottom or top of the sample. This means the magnetization is deflected slightly out-of-plane [Wen17]. Hereby, an anomalous Hall effect is generated that is proportional to the z-component of the magnetization (see Fig. 2.6b), and simply measurable as a voltage $U_{\mathrm{AHE}}$. If the current is an ac current at low frequencies ($\ll$ GHz), then a second harmonic becomes observable [Hay14]. This second harmonic shows a characteristic dependence on the magnetization orientation which we can get from the addition theorems. In addition, the sensitivity of the anomalous Hall voltage $U_{\mathrm{AHE}}/H_z$ is measured separately to evaluate the spin Hall angle [Wen17].

All the mentioned methods are relatively complex and time-consuming because applying contacts always involves contact resistances which are not so easy to measure. In case of spin pumping/FMR and harmonic Hall measurements, a micro structuring by lithography is necessary. Due to the complex preparation, the methods are difficult to implement when many samples have to be measured. This is why, it is desirable to have a method which is suitable for fast screening of many samples, that is contact-free and without micro structuring.
Here, we use terahertz emission spectroscopy, that provides the spin-to-charge conversion efficiency relative to a reference sample and gathers all the mentioned requirements.

## 2.7. Terahertz measurement of the SHE

The idea of this method is to measure spin currents with an optical method on ultra-fast timescales. It uses the ultrafast SDSE or SSE to generate spin currents inside a ferromagnetic conducting or insulating material. The THz emission spectroscopy from photoexcited ferromagnetic/non-magnetic (FM|NM) thin-film bilayers lends itself to characterize the NM layer spin Hall conductivity.

### 2.7.1. THz emission from thin-film bilayers

The emission of THz radiation from thin-film bilayers is based on two effects. First, the ultrafast spin-dependent Seebeck effect, which generates a spin current by optical pumping a FM|NM stack. Second, the ultrafast inverse spin Hall effect, which converts the spin current into a transverse charge current (see Fig. 2.7).
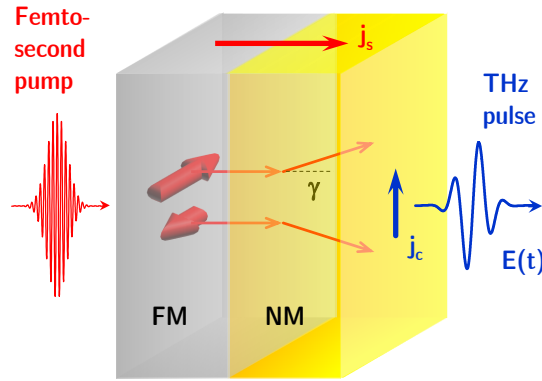
**Principle**



Figure 2.7.: **Terahertz emission of thin metal bilayers**. A femtosecond laser pulse excites the sample which consists of a ferromagnetic (FM) and a non-magnetic (NM) layer. The spin-dependent Seeback effect converts the absorbed power into a spin-dependent charge current $j_s$ in the FM layer. This current is transformed by the spin Hall effect into a transverse flowing charge current $j_c$ in the NM layer. Due to the ultrashort pump and fast relaxation, $j_c$ is acting like a time-dependent electric dipole emitting terahertz electromagnetic radiation. Figure from [Sei16] with permission of T. Seifert.

In more detail, a femtosecond laser pulse is incident on the sample and excites electrons to states above the Fermi level. Spin-up and spin-down electrons have different transport properties, which results in a spin current along the sample normal. The reason for the spin polarization lies in the different electron lifetime, band velocity and density of spin-up and spin-down electrons in typical FM materials. The generated spin current is injected into the NM layer. Here, the inverse spin Hall effect deflects electrons with respect to their spin state under an angle $\gamma$, called spin Hall angle, in opposite directions. The conversion of the spin current into a transverse charge current takes place instantaneous within our time resolution. In total, the pure charge

current is a time-dependent electric dipole which radiates an electromagnetic field with a polarization plane perpendicular to the external magnetic field. In addition, the emitted terahertz radiation is broadband due to the ultrashort excitation pulse (10 fs) and short lifetimes of metal electrons ($\sim 100$ fs) [Zhu06].

## THz emission model

We need to find a model that links the emitted THz electric field $E$ to the generated spin current. Such a model was derived by Seifert *et al.* [Sei16] and yields

$$E(\omega) = Z(\omega) \cdot e \int_0^d \mathrm{d}z \, \gamma(z) j_\mathrm{s}(z, \omega) \tag{2.7.1}$$

This can be understood as a generalized Ohms law with an impedance $-Z(\omega)$ of the sample which describes the outcoupling efficiency of the emitted THz electric field [Sei16]. Please see the appendix A.1 for more detailed information on the derivation of the model. The impedance can be written as

$$\frac{1}{Z(\omega)} = \frac{n_1(\omega) + n_2(\omega)}{Z_0} + \int_0^d \mathrm{d}z \, \sigma(z, \omega) \tag{2.7.2}$$

which includes propagation and reflection/echos of the generated terahertz field inside the sample [Sei16]. We note that this equation is only valid in the thin-film limit. This limit is given when the total film thickness is much smaller than the wavelength and attenuation length of the participating waves.

The spin current is proportional to the absorbed pump light energy density that is indicated by linear pump fluence on the THz emission amplitude. This explains the factor $A/d$, where $A$ represents the pump light absorptance and $d$ is the total stack thickness [Sei16]. The total thickness of the sample stack has an influence on the THz emission amplitude, because the factor $A/d$ decreases with increasing $d$ and because the impedance decreases with increasing thickness. In addition, it has to be considered, that the spin current density $j_\mathrm{s}(z)$ inside the NM layer is spatially dependent. According to [Sei16], we take

$$j_\mathrm{s}(z) = \tanh\left(\frac{d_\mathrm{NM}}{2\lambda_\mathrm{rel}}\right) \tag{2.7.3}$$

for this dependence into account with $\lambda_\mathrm{rel}$ describing the electron velocity relaxation length. Detailed information on the procedure how to derive this model are provided in [Sei16].

Putting all these assumptions together, we obtain

$$E(\omega) \propto \frac{A}{d} \cdot Z(\omega) \cdot \gamma \cdot j_\mathrm{s}^0 \cdot \lambda_\mathrm{rel} \cdot \tanh\left(\frac{d_\mathrm{NM}}{2\lambda_\mathrm{rel}}\right) \tag{2.7.4}$$

to model the relation between emitted terahertz electric field per incident fluence and
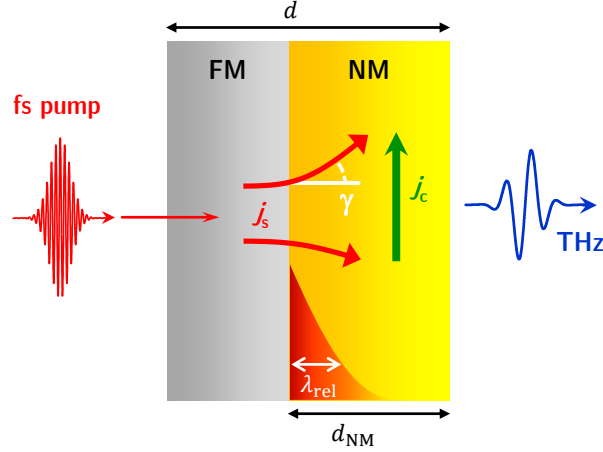
**Figure 2.8.: Terahertz emission model.** The optical femtosecond pump is partialy absorbed by the thin-film sample with total thickness $d$. Due to the pump induced non-equilibrium, the spin-dependent Seebeck effect generates a spin current $\boldsymbol{j}_\mathsf{s}$. In the course of relaxation $\lambda_\mathsf{rel}$, the spin current is injected from the NM to the FM layer. Here, the current $j_\mathsf{s}$ is transformed into a transverse charge current $\boldsymbol{j}_\mathsf{c}$ by the inverse spin Hall effect with the efficiency $\gamma$. THz radiation is generated, and coupled out of the sample with a impedance $Z_\mathsf{eff}$. Figure redrawn from [Sei16].

the spin current generated by photo excitation. Here, $j_\mathsf{s}^0$ is the spin current density which is injected into the NM layer normalized to the pump power.

The THz emission spectroscopy is a semi quantitative method. To obtain finally absolute values for the spin Hall angle, a reference measurement with a well-known sample is needed. To determine the spin Hall angle $\gamma$ or the spin Hall conductivity $\sigma_{\mathrm{SH}}$, we need to know the THz electric field $E_{\mathrm{THz}}$, how much energy of the optical pump light $A$ is deposited in the sample, what is the effective impedance $Z_{\mathrm{eff}}$ of the thin-film stack and what is the relaxation length $\lambda_{\mathrm{rel}}$ (see Fig. 2.8). The thicknesses $d$ and $d_{\mathrm{NM}}$ of the sample are known from the sample growth process. Finally, we need information about the spin current $j_\mathsf{s}^0$.

## 2.7.2. Impedance measurement by THz transmission

As mentioned in the last section, we need a method to measure the impedance $Z_{\mathrm{eff}}$ of a thin-film sample. The solution is to perform two terahertz transmission measurements through the sample. First, measure the THz transmission through the sample stack on the substrate $E_{\mathrm{sample}}$ and second, we measure the THz transmission through the substrate only for referencing $E_{\mathrm{ref}}$ (see Fig. 2.9).

For information about the derivation of the following equation, please see appendix A.2. We obtain by calculating the ratio of the measured THz transmission curves

$$\frac{E_{\mathrm{sample}}(\omega)}{E_{\mathrm{ref}}(\omega)} = \frac{1}{1 + \frac{Z_0}{n_1+1} \int_0^d \mathrm{d}z'\, \sigma(z',\omega)}. \qquad (2.7.5)$$

We call this ratio the transmission function $t(\omega)$ and the integral in equation 2.7.5
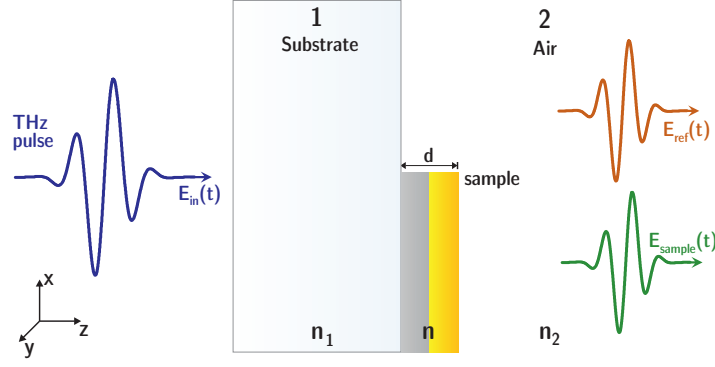
**Figure 2.9.: Terahertz transmission through a thin film sample**. The transmitted field is measured through substrate and sample and for referencing only through the substrate.

becomes a sum of the conductivities $\sigma_j$ for each layer $j$ in case of a multilayer sample, which reads

$$t(\omega) := \frac{E_{\text{sample}}(\omega)}{E_{\text{ref}}(\omega)} = \frac{1}{1 + \frac{Z_0}{n_1+1} \sum_j \sigma_j(\omega)d_j}. \qquad (2.7.6)$$

It is possible to extract the conductivity of the sample at THz frequencies with the above shown formalism. It would be helpful if we could calculate the conductivities at dc to compare them to dc measurement results. For this purpose, we use the Drude model to get information about the Drude relaxation time $\tau$ and $\sigma_{\text{Drude}}$ from the NM metal layer and we compare the THz conductivity $\sigma(\omega)$ with $\sigma_{\text{Drude}}(\omega)$. To fit the THz conductivity data, we use $\sigma_{\text{dc}}$ and $\tau$ as fit parameters (see Eq. 2.4.2). In addition, a small substrate thickness variation $\Delta d_{\text{sub}}$ between sample and reference has to be considered in the fitting process [Kre18].

# 3. Experimental details

## 3.1. Terahertz spectrometers

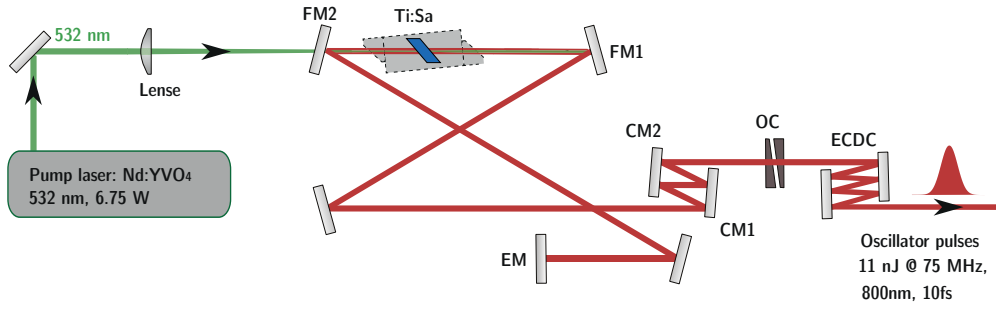### 3.1.1. Laser system: High repetition rate laser oscillator



Figure 3.1.: **High repetition rate laser oscillator**. A ND:YVO$_4$ laser emitting at 532 nm pumps the titanium-doped sapphire crystal (Ti:Sa) inside the oscillator cavity. The output coupler (OC) and the end mirror (EM) represent two of the basic elements of the optical cavity. Two mirrors (FM1/2) focus the high intensities into the Ti:Sa. By Kerr lens mode-locking femtosecond, laser pulses are generated. The pulse dispersion is controlled by two chirped mirrors (CM1/2) and an external cavity-dispersion control (ECDC). Figure from [Bra16b] with the permissions of L. Braun and S. Mährlein.

The central device used in this thesis is a titanium-sapphire (Ti$^{3+}$Al$_2$O$_3$, short Ti:Sa) laser oscillator with MHz repetition rate. The oscillator cavity is a *FEMTOSOURCE M1* manufactured by the FEMTOLASERS Produktions GmbH (now part of Spectra-Physics).

The Ti:Sa crystal is pumped near its absorption maximum with 532 nm continuous wave (cw) light [Rul05] by a Coherent Verdi V10 at an output power of 6.75 W. The pump laser consists of two solid state laser diodes emitting at 808 nm. They are pumping a neodymium-doped yttrium orthovanadate crystal which has an active laser transition at 1064 nm. By using a lithium triborate (LBO) crystal an efficient second harmonic generation is performed to reach the required output wavelength of 532 nm [Eic10]. Figure 3.1 shows the scheme of the MHz oscillator laser to provide femtosecond laser pulses.

The pump light is focused into the water cooled Ti:Sa crystal. Femtosecond laser pulses are generated by the common method of Kerr lens mode-locking [Rul05] and the broad gain bandwidth of the active laser medium, the Ti:Sa crystal.

The Kerr lens mode-locking is based on the self focusing effect in Kerr media. In such media, higher intensity modes are more focused than lower ones. This leads to an amplification of the most intense modes [Sei17c]. The outcoupled light has a central wavelength of around 800 nm. The ultrashort laser pulses have a duration of 10 fs and an energy of 11 nJ at a repetition rate of 75 MHz. The dispersion of the laser pulses is compensated by a pair of chirped mirrors (CM1/2) and an external cavity-dispersion

control (ECDC). Further information on this laser system can be found in [Bra16b].

## 3.1.2. Generation of THz radiation

In this section, two different concepts for THz radiation generation are presented. At first, the common method of optical rectification in transparent electro-optic crystals and the second method is a new approach to generate terahertz electric fields. We use thin ferromagnetic/non-magnetic films for THz emission and call the optimized structure spintronic terahertz emitter (STE).

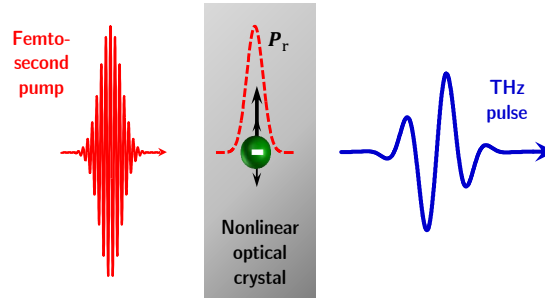### Optical rectification in transparent, electro-optic crystals



Figure 3.2.: **Optical rectification**. A femtosecond pulse is incident onto a nonlinear, non-inversionsymmetic crystal. The rectified component $P_r(t)$ of the induced electronic polarization follows the envelope of the pulse intensity (red curve inside the crystal). A terahertz pulse is emitted by the component $P_r(t)$ into the optical far-field. Figure redrawn from [Kam13b]

The generation of electric fields at THz frequencies in transparent, electro-optic crystals is based on optical rectification. This process requires a non-centrosymmetric crystal with second-order nonlinear susceptibility (nonzero $\chi^{(2)}$) [Tom13]. In such a medium, processes like sum frequency generation (SFG) and optical rectification are principally possible. When we pump the crystal with a continuous wave laser beam, the crystal produces a rectified dc electric field, which is proportional to the pump intensity [Tom13]. In contrast, when illuminating the crystal with ultrashort broadband pulses of femtosecond duration, the electrons inside the crystal follow the electric field of the pulse and act like an electric dipole that re-emit radiation. In a higher-order response the electrons follow the envelope of the driving pulse (see Fig. 3.2). The optical rectification process mixes pairs of frequencies within the pump pulse spectrum which results in the re-emission of pulses carrying frequencies in the THz regime. We note that the THz pulse in the far-field is the second derivative of that time-dependent polarization.

### Spintronic terahertz emitter

The THz generation process, presented here, make use of the emission of terahertz radiation from thin-film stacks. In principle, we transform our characterization tool
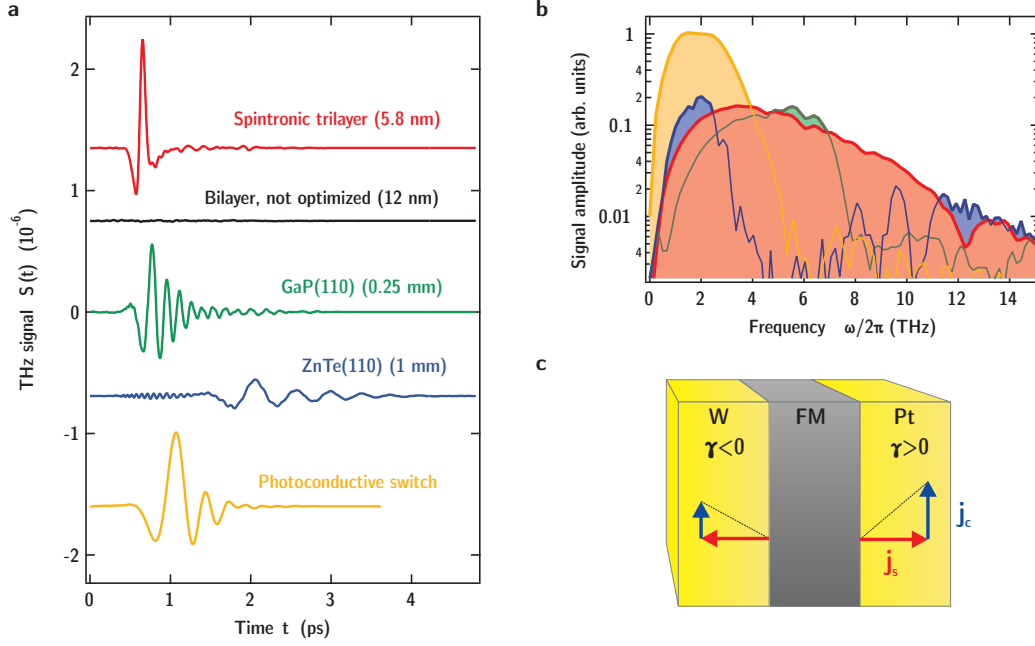
**Figure 3.3.: Spintronic tearhertz emitter. a**, Comparison of the spintronic terahertz emitter trilayer (red) to the not optimized bilayer version of itself (black), to standard transparent electrooptic cyrstals GaP and ZnTe (green and blue), and to a photoconductive switch (yellow) in the time-domain. **b**, Spectra of the terahertz emitters shown in **a**. The optimized spintronic trilayer outperforms standard emitters in certain spectral ranges. **c**, Sample structure of the spintronic terahertz emitter trilayer. Pt and W are used as non-magnetic layers. W has an opposite spin Hall angle compared to Pt. We take advantage of the electrons propagating forward and backward. Thereby, it is possible to increase the amplitude of the emitted terahertz radiation by a constructive superposition of the two spin Hall currents. Figures **a** and **b** from [Sei16] with the permission of T. Seifert, Figure **c** redrawn from [Sei16].

"THz emission spectroscopy" into an application.

So, the underlying physical principles are the spin-dependent Seebeck effect and the ultrafast inverse spin Hall effect. As explained in detail in chapter 2.7.1, the SDSE generates an out-of-plane spin current and the SHE is responsible for the conversion into a transverse charge current.

Fig. 3.3c shows the optimized structure: a 5.8 nm trilayer consisting of two non-magnetic and one ferromagnetic layer in between (NM|FM|NM). We use CoFeB of 1.8 nm thickness for the FM layer and so far the optimum NM materials turned out to be Pt and W with thicknesses of 1.5 nm each. By using a trilayer with NM materials having an opposite sign in the spin Hall angle, we are making use of both spin currents superpositioning constructively with each other. In addition, we magnetize the FM layer in-plane with an external magnetic field to enhance the amplitude of the emitted electric field.

The STE has several advantages compared to standard crystalline THz emitters. Fig. 3.3a shows the STE in comparison with electro-optic crystals GaP and ZnTe, and a photoconductive switch. We recognize that the STE has a comparable THz electric field amplitude to the other shown emitters. By Fourier-transforming the

time-domain data, we gain insights on the spectral behavior of the THz emitters (see Fig. 3.3b). The STE has a broadband spectrum without gaps. In addition, such an emitter made of a simple thin-film structure are low cost compared to electro-optic crystals. In summary, the spintronic terahertz emitter exhibits a comparable or even better efficiency than standard emitters in certain spectral ranges. Recently, it was shown, that the STE is also scalable [Sei17a]. More details on the spintronic terahertz emitter are provided in [Sei16].

### 3.1.3. Detection of THz electric fields

Terahertz spectroscopy in the time-domain opens up the possibility to measure simultaneously amplitude and phase of the THz electric field. An effect which is able to provide the detection of both components, is the Pockels effect, also called linear electro-optic effect [Dex08]. The response of this linear electro-optic effect is a change in the refractive index of a medium, that goes linearly with the applied electric field [Boy08, Sei17c]. To exhibit a linear electro-optic effect, a medium has to have a broken inversion symmetry, which is given by a high second-order nonlinearity $\chi^{(2)}$ [Dex08]. Common transparent, electro-optic crystals such as ZnTe or GaP are suitable for THz detection.

In detail, the THz field modulates the refractive index of the nonlinear crystal which is equivalent to the statement that the medium becomes birefringent. Then, the co-propagating gate pulse experiences this induced birefringence which is proportional to the THz electric field [Sei17c]. The result is a polarization change of the gate pulse from initially linear to elliptical. In summary, one can imprint the electric field information of the THz pulse on the polarization state of the optical gate pulse at a certain time delay between THz and gate pulse. The method to measure the polarization state will be shown in the following section 3.1.4.

### 3.1.4. THz spectrometer setups

We are able to perform two different measurement methods in our terahertz spectrometer setup: THz emission e.g. from a thin-film sample and THz transmission through such as sample.

**THz transmission and emission spectrometer**

The laser beam is separated by a beam splitter into a pump and a gate pulse with a ratio of 80:20. The pump beam is modulated by an optical chopper at 35 kHz. This high modulation frequency was chosen to detect the THz signal far away from the $1/f$ noise. We use a second modulator at 25 Hz for delaying the pump beam with respect to the gate beam. This so-called shaker consists of a retro-reflector mounted on a membrane that is shaking back and forth. The shaker achieves a maximum
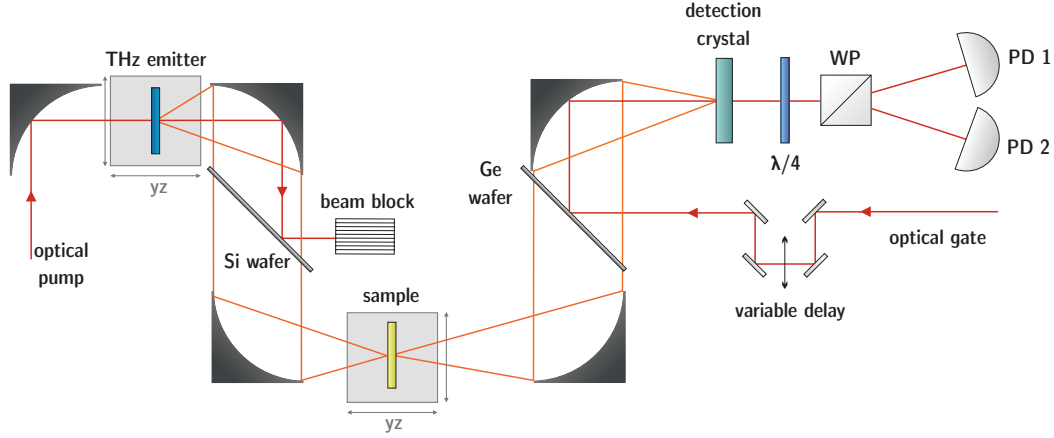
**Figure 3.4.: Terahertz spectrometer**. The spectromter consists of two focal positions. In THz transmission mode, an emitter is placed in the first focus, the sample in the second one. In emission mode focus one is unused while the sample is pumped in the second focus. In both modes optical light pulses are focused by off-axes parabolic mirrors into the terahertz emitter respectively the sample where the emission of THz radiation is triggered. A subsequent off-axis parabolic gold mirror collimates the emitted THz pulses. The co-propagating pump beam is blocked by a Ge wafer that is mostly transparent for THz radiation. The optical gate beam is introduced into the detection by the Ge wafer. THz and gate beam are spatially and temporally overlaped in the detection crystal where the THz electric field information is tranfered into the polarization state of the gate pulse. This polarization state can be detected by a pair of balanced photodiodes. Figure redrawn from [Bra16b].

pump-probe delay of 50 ps. With this modulation method we are instantly able to see the signal on a computer screen in contrast to the classical step-scan technique for varying the pump-probe delay. The rough time delay is set by a motorized linear translation stage in the pump beam. By using a $\lambda/2$ or $\lambda/4$ waveplate we manipulate the incoming pump pulse polarization depending on the requirements of the used emitter/sample.

As described in chapter 2.7.2 we use terahertz transmission measurements to gain information about the impedance of the sample stack. A schematic of the setup is shown in Fig. 3.4. We focus the optical pump beam with an uncoated 90°-off-axis parabolic gold mirror. The THz emitter sits in the focus on a two axes translation stage. The bandwidth of the emitted THz electric field depends on the used emitter. The emitted THz pulses are collimated by a subsequent parabolic gold mirror and a second focus for the sample is generated by another parabolic gold mirror. For positing the sample, another two axes linear translation stage is used.

Between focus one and two, a silicon wafer is placed in the pump-wavelength Brewster angle to let the THz radiation transmit and to reflect the optical pump into a beam block. We measure the transmission of the THz pulses through the sample. For referencing we need to measure the THz transmission through the substrate only. We use a motor which shifts the sample perpendicular to the sample normal to a nearby, in the same plane mounted additional substrate. We repeat this procedure of measuring only the substrate and in a second measurement substrate plus thin-film several times

for a better statistics. In an optimum case, only one half of the substrate is covered by the thin-film stack.

We always used the spintronic terahertz emitter for the performed THz transmission measurements. All THz transmission measurements were done at room temperature. The TaAu and $WO_x$ series were measured under a dry nitrogen atmosphere, while the AuPt series was measured under ambient conditions due to a lack of nitrogen.

For the THz emission mode the first focus is simply unused. The sample is placed in the second focus, where the optical pump beam triggers the terahertz emission process. In-plane magnetic fields are introduced via permanent magnets on top or on the side of the sample. All THz emission measurements were performed at room temperature under ambient conditions. The emitted or transmitted THz electric field is collimated by a forth, subsequent parabolic gold mirror with same focal length as the foregoing mirror. Hereby, the THz pulses are guided to the detection unit.
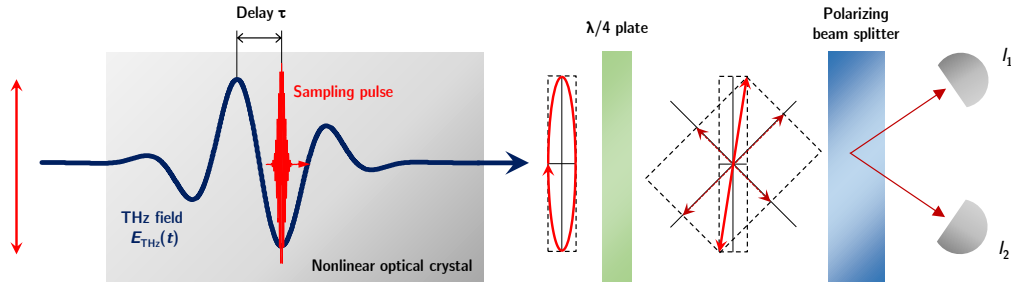
## THz detection unit



Figure 3.5.: **Electro-optic sampling**. Terahertz pulse and optical probe pulse are focused into a nonlinear optical crystal. The THz electric field changes the polarization state of the optical probe pulse by modulating the refractive index of the crystal. The initially linearly polarized probe pulse is leaving the crystal with an elliptical polarization. This ellipticity is transformed into rotation change of the ellipse by a $\lambda/4$-plate. A polarizing beam splitter separates spatially the two orthogonal components, so they can be detected by two balanced photodiodes. Figure redrawn from [Bra16b] with the permission of L. Braun.

The optical probe pulse is coupled into the setup via a silicon/germanium wafer which reflects the co-propagating optical pulse and is transmissive for THz frequencies (see Fig. 3.4). Behind the wafer, the THz electric field and the gate beam are co-propagating. A further parabolic mirror is used to focus THz and probe beam into the detector. A nonlinear crystal is used for detection via the linear electro-optic effect. All THz emission experiments were detected by a 1 mm zinc telluride (ZnTe) in (110)-orientation. For detection in the THz transmission studies, we chose a 250 µm GaP (110) crystal.

The crystal transfers the information of the terahertz electric field into the polarization state of the sampling pulse. The initially linearly polarized gate beam becomes

elliptical. This ellipticity of the sampling pulse is proportional to twice the THz electric field at a given pump-probe delay. We are making use of a $\lambda/4$ waveplate which tranforms the induced ellipticity into a rotation change of the ellipse (see Fig 3.5). In our setup, a combination of a non-polarizing beam splitter and a $\lambda/2$ waveplate is used to separate the two perpendicular polarized components, which has the same effect as a polarizing beam splitter. The small gate-pulse-ellipticity change is measured by an intensity change between two balanced photodiodes [Sei17c]. The signal depending on the delay $\tau$ reads

$$S(\tau) := \frac{I_1 - I_2}{I_1 + I_2}, \tag{3.1.1}$$

where $I_{1,2}$ are the respective photocurrents of the photodiodes. The advantage of these two balanced photodiodes lies in the fact that the signal-to-noise ratio can be considerably improved by substracting the intensities on the photodiodes without presence of a THz electric field [Sei17c].

We note that the signal amplitude and bandwidth depend on the electro-optic crystal material and its thickness due to different phase matching conditions for different frequency ranges. Phase matching means that the phase velocity of the THz pulse is equal to the velocity of the optical pulse envelope [Dex08]. Low frequencies are better phase matched in thick crystals which leads to higher amplitudes in the low frequency range. In contrast, the phase matching in thin crystals works more efficient for higher frequencies which results mostly in lower amplitudes but an extended frequency detection sensitivity.

Finally, the acquisition of the photodiodes' voltage signal is done by a DAQ card and LabVIEW. More details on the data acquisition process are provided in [Bra16b].

## 3.2. Sample details and characterization

### 3.2.1. Sample structure and growth

In this section, we will provide basic information about the sample structure and deposition parameters which are common for all studied samples. Specific details on the sputtering parameters or differences in the structure can be found the the respective sections in chapter 4.

The samples for THz spin Hall characterization, provided by the group of Markus Meinert from the university of Bielefeld, are grown on fused silica substrates with dimensions of 10 mm × 10 mm and 500 µm thickness. Magnetron sputtering technique was used to deposit thin-films of cobalt-iron-boron (CoFeB) and a non-magnetic heavy metal respective binary metal alloy. A Bestec 2" confocal magnetron co-sputtering system was used. For more information about the magnetron sputtering process, please see [Ohr02].
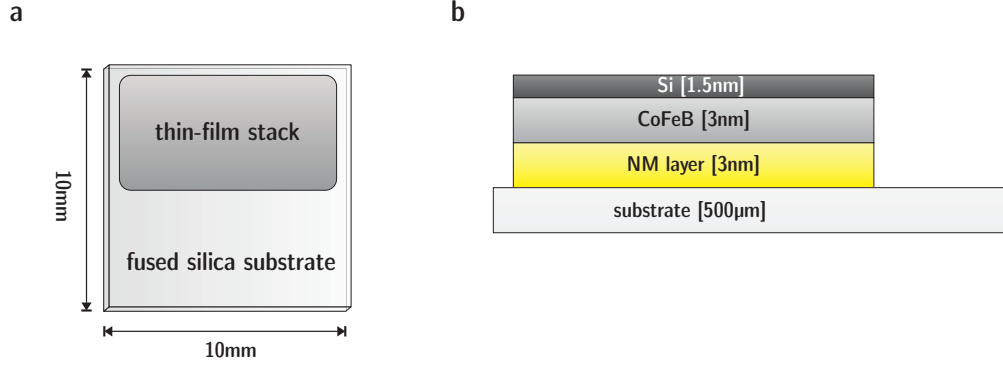
**Figure 3.6.: Sample structure.** **a**, The fused silica substrate (10 mm × 10 mm) is only partially covered by the thin-film stack to perform easily terahertz transmission measurements. **b**, Side view of the sample. A 1.5 nm-thick silicon layer prevents the subjacent bilayer from oxidization. Figure redrawn from [Pra17].

For reference purposes, when performing THz transmission measurements, only one half of the substrate is covered by the thin-film (see Fig. 3.6a) using a metallic mask during the sputtering process. All substrates were cleaned before depositing the thin-film stack on top. The best cleaning results was achieved using an etching technique. Hereby, a sputtering gas mixture of $Ar/O_2$ with ratio of 2:10 was applied to clean the substrate surface. The CoFeB layer was dc-sputtered with a pressure of $1.5 \cdot 10^{-3}$ mbar, an Ar flow rate of 10 sccm (sccm = standard cubic centimeters per minute) and a sputtering power of 25 W. The deposition rate was 0.24 Å/s. All sample stacks are capped by a 1.5 nm thick Si layer to prevent the CoFeB layer from oxidation (Fig. 3.6b). The capping layer was rf-sputtered with a sputtering pressure of $2.0 \cdot 10^{-3}$ mbar, an Ar flow rate of 10 sccm, a sputtering power of 50 W and a deposition rate of 0.16 Å/s. X-Ray reflectivity measurements conducted by the group of M. Meinert showed that the Si layer achieves its prupose because only 0.5 nm is oxidized [Pra17].

The CoFeB|Pt samples with varying Pt and CoFeB thicknesses are prepared by the group of Mathias Kläui from the Johannes Gutenberg University in Mainz. They used a Singulus Rotaris UHV deposition system to fabricate thin-film stacks. Here, the whole substrate area is covered by the sample stack. And we have to note that the stacking order is reversed compared to the in Fig. 3.6b shown one.

### 3.2.2. Electrical conductivity measurement

All dc-measurements of the electrical resistivity were conducted by the group of Markus Meinert. They performed a four-point resistance measurement on equivalent AuPt, TaAu and $WO_x$ samples with 40 nm thickness on $Si|SiO_x$ substrates.

In this technique four needles in one row with equidistant spacing are contacted to the sample surface. By applying a current to the outer needles, they are able to measure a voltage between the two inner needles. Using the well known relation

$$R = \frac{U}{I} \tag{3.2.1}$$

gives the resistance for a certain current. Furthermore, the resistivity is obtained by

$$\rho = \frac{\pi d \cdot R}{\ln(2)} \tag{3.2.2}$$

and a parallel circuit theory with known resistivity for CoFeB. The analysis gives finally the resistivity of the NM layer. The conductivity $\sigma$ of the NM layer is simply the inverse of $\rho$

$$\sigma = \frac{1}{\rho} \tag{3.2.3}$$
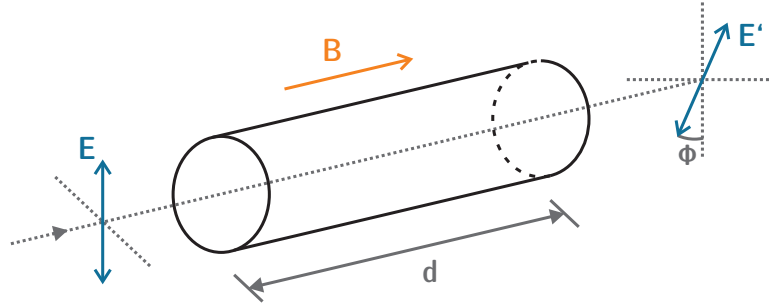
### 3.2.3. Magneto-optic characterization



Figure 3.7.: **Faraday effect**. Linearly polarized light is transmitted through a magnetized material. Due to the magnetization inside the material, the polarization is rotated by an angle $\phi$. Figure redrawn from [Hai17].

To study the interaction of optical light with matter, here, we focus on magnetic materials, the class of magneto-optical effects are commonly used. The light affects the magnetic state, and the electronic structure of the material has to be involved in the consideration. In addition, the polarization state of the light plays an important role. The magneto-optical effects are basically categorized by their fundamental geometries: in reflection geometry the effect is called magneto-optical Kerr effect (MOKE) and the Faraday effect is present in transmission geometry.

MOKE is in principle an anomalous Hall effect at finite frequencies, where a linearly polarized pulse drives a current which is transferred into a transverse current. The latter acts like an time-dependent electric dipole and emits radiation. This emission changes the light polarization behind the medium.

In this thesis, the Faraday effect is more in the focus to measure changes in the magnetization. It was discovered in 1845 by Michael Faraday and is described as follows. Linearly polarized light is transmitted through a magnetized material whereupon the sample is magnetized along the propagation direction of the light. The polarization undergoes a rotation in the medium (see Fig. 3.7). To quantify this rotation angle $\phi$,

it reads

$$\phi = V(\omega) \cdot B \cdot d \qquad (3.2.4)$$

with the magnetic field $B$, the length of the medium $d$ and the Verdet constant $V$, which is dependent on the temperature, the material properties and the light wavelength [Hai17]. The rotation sense of the Faraday angle $\phi$ depends on the magnetic field direction [Sug00].

We have to note that in principle the Faraday effect is not suitable for in-plane magnetized samples. But by tilting the sample with respect to the incident optical beam, a part of magnetization is projected along the propagation direction of the optical beam. Thus, the Faraday effect gets visible even in in-plane magnetized samples.

All magneto-optical measurements, which were performed in this thesis, were done always in the Faraday geometry due to space limitations in the setup. Fig. 3.8 shows partially the standard THz emission setup, into which we integrated the setup for Faraday measurements. It consists of two polarizers, a photoeleastic modulator (PEM), a lens and a mirror in front of the Ge wafer, as well as a photodiode. As shown in Fig. 3.8 the first polarizer is placed in front of the sample to set an incident polarization state. The Faraday effect rotates the polarization proportional to the magnetization change in the tilted sample. This rotation is analyzed by the second polarizer which is rotated by 45° compared to the first one. The PEM modulates the signal at 50 kHz by changing the refractive index of a fused silica crystal that influences the polarization state of the through-propagating beam. That kind of modulation is needed to get rid of the $1/f$ noise. Further details on the operation mode of PEMs are provided in [Bad90]. The polarization change is detected as a intensity varying signal by a photodiode and a lock-in amplifier.
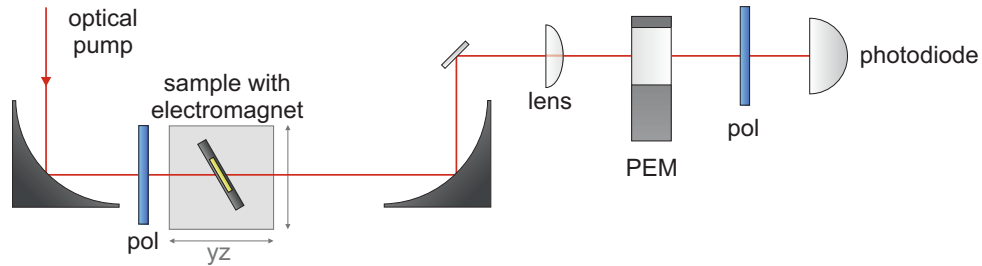


**Figure 3.8.: Faraday setup**. THz emission setup with integrated possibility to measure Faraday signals. The setup consists of a pair of polarizers: the first sets a well defined polarization state and the second analyzes the Faraday rotation $\phi$. The Faraday signals are modulated at 50 kHz with a photo elastic modulator (PEM) and detected by a photodiode.

## 3.3. Sample magnetization control

### 3.3.1. Electromagnet

Here, we introduce the first prototype of a home-made quadrupole electromagnet. The development of such a magnet system is generally motivated by the request to have the possibility to control contact-free the polarity and polarization plane of the spintronic terahertz emitter. As shown in Fig. 2.7, the emitted THz electric field of the STE is always linear polarized with a polarization plane perpendicular to the external-magnetic-field direction in the case of pumping the emitter with linearly polarized light. This dependence permits a polarity and polarization plane control by manipulating the direction of the external magnetic field. We realize this with an electromagnet made out of four coils and a ferrite ring as shown in Fig. 3.9a.

For the development, we require small solenoids to fit into our reflection and transmission geometry setups and a magnetic field strength of more than $10\,\mathrm{mT}$ at the sample position. In addition, the electromagnet should be able to work in a dc mode to switch between parallel and perpendicular in-plane magnetic fields and in an ac mode, where we want to apply time-dependent currents to the coils to rotate finally the in-plane magnetization of the sample.

The first step is the realization of a static magnetic field. Fig. 3.9a depicts the coil orientation which has its windings perpendicular to the requested magnetic-field direction. We choose this configuration because we get the strongest fields perpendicular to the winding of the coil. Oppositely mounted coils are electrically coupled for acting like one coil. The sample position is acting like an air gap, in which the magnetic field lines should close themselves to form a homogeneous magnetic field.



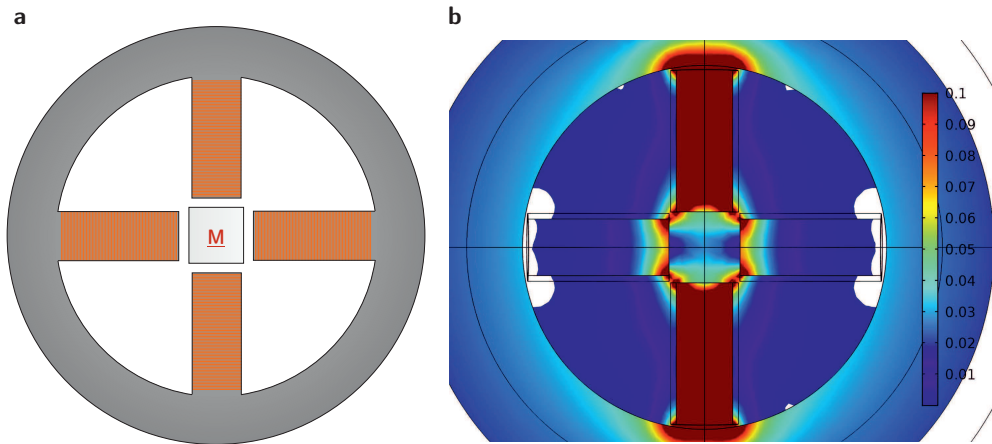**Figure 3.9.: Geometry of an electromagnet for polarization and polarity control of thin FM|NM samples**. **a**, First prototype for an electromagnet using four cylindrical solenoids to magnetize the centered sample in different in-plane directions. **b**, COMSOL simulation of the magnetic field in the realized geometry. Zoom in to the sample position. Fig. **b** provided by Seyed Mohammadreza Rouzegar.

The outer ferrite ring with a high permeability $\mu_r$ is used to close a second air gap which lies between the outer edges of a pair of coils. By using the ferrite ring, the magnetic field lines are efficiently guided because materials with high permeability act like a conductor for magnetic fields.

Fig. 3.9b shows a COMSOL simulation of the constructed prototype geometry to confirm the measured maximum magnetic field between two coils. We measured a magnetic field of 16 mT at 14 A input current. The performed simulation, conducted by Seyed Mohammadreza Rouzegar from the FU Berlin, exhibits a magnetic field of 27 mT. Indeed, the simulation considers no losses that may explain the difference to the measured value. Furthermore, the simulation shows that the generated field is not homogeneous. We explain this by the fact that the dimension of the air gap is in the same order as the diameter of the coils. But besides this, the expected linear behavior between the magnetic field and the input current is given.

# 4. THz spin Hall characterization of spintronic metals

## 4.1. Motivation

In this chapter, we use terahertz emission spectroscopy as an all-optical characterization tool for spintronic materials. In this connection, we are focusing on the characterization of the spin Hall effect in different compounds. THz emission spectroscopy facilitates several advantages compared to common electrical measurement techniques such as working on ultrafast timescales and measuring contact-free without any need for microstructuring.

A number of pure materials and a few compunds such as FeRh, GdFe, and DyCo have been analyzed by Seifert *et al.* [Sei16] to optimize the THz emission amplitude. Here, we go further to metallic binary alloys and doped systems. We focus on promising high-spin-orbit materials that were already studied by ferromagnetic resonance measurements or theoretical simulations in other groups. By studying complex compounds, we make use of the advantage of terahertz emission spectroscopy to rapidly screen many samples with different material parameters. The overall goal is to explore promising materials concerning their spin-to-charge conversion efficiency with variation of the stoichiometry in a wide concentration range.

## 4.2. Metallic binary alloys

An interesting class of materials are binary alloys, where the impurity concentration is varied. By introducing impurities, the spin Hall effect scattering mechanisms such as the skew scattering may be positively influenced to enhance the spin-to-charge conversion. The importance of efficient spin-to-charge converting materials for potential spintronic applications has been pointed out in the previous chapters of this thesis.
In this section, we characterize two different metallic binary alloys. The method of characterizing spintronic materials by terahertz emission spectroscopy is demonstrated on the basis of a gold-platinum-alloy $Au_xPt_{1-x}$ (AuPt). The idea to study AuPt is taken from Obstbaum *et al.* [Obs16], in which they investigated this binary alloy on a theoretical and experimental basis.
The second binary alloy which is presented here, is tantalum-gold $Ta_xAu_{1-x}$ (TaAu). This material has already been studied by Laczkowski *et al.*, but only in a limited range up to 30 % of Ta concentration [Lac17]. In this thesis we extend our studies to the whole relative concentration range in TaAu.

### 4.2.1. Gold-platinum-alloy $Au_xPt_{1-x}$

**Sample preparation**

Basic information on the sample structure and common film deposition parameters can be found in section 3.2.1. Here, we give some more details on the studied samples. The binary alloy layers $Au_xPt_{1-x}$ were dc-magnetron-sputtered at a pressure of $2 \cdot 10^{-3}$ mbar with an Ar flow rate of 10 sccm. Two sputter sources with varying sputtering powers were used to compose a set of ten binary alloy samples with tuning stoichiometry.

**Raw data**

Three different types of measurements were performed on the samples: THz emission, THz transmission and pump-light absorptance measurements. The THz emission signal of all the samples in the series flips with the reversal of the external magnetic field, which is shown for one typical sample in Fig.4.1a. The signal flip indicates a magnetic origin of the signal.
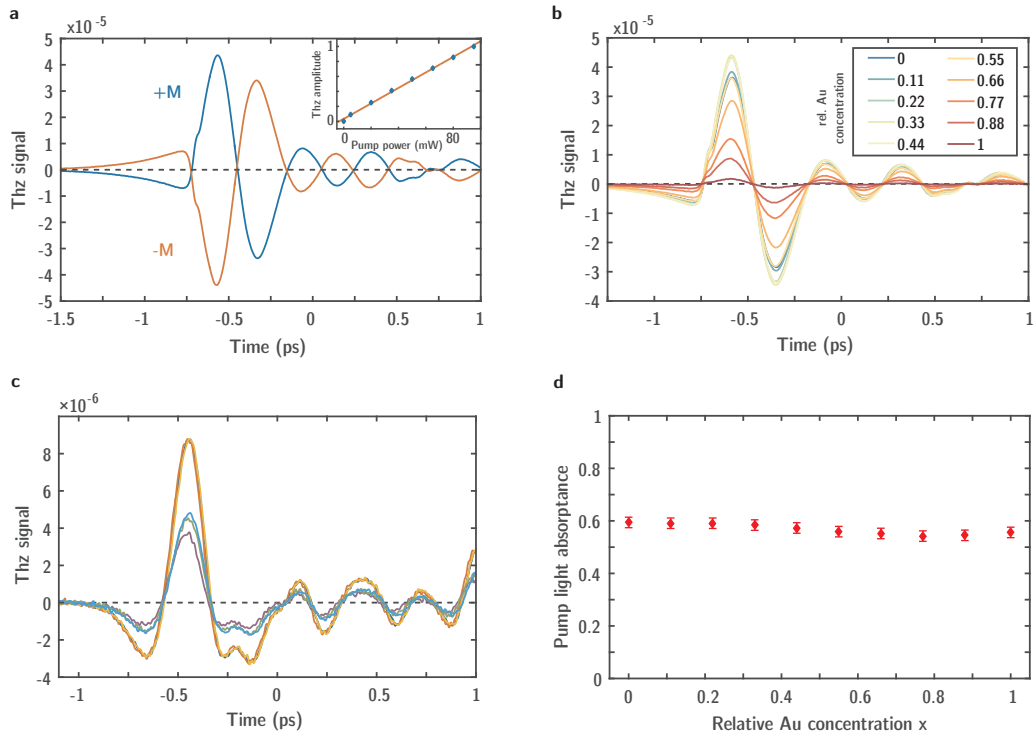


**Figure 4.1.: Raw data from $Au_xPt_{1-x}$. a**, THz signals from one composition with opposite magnetic field directions ($\pm$M). The sign of the THz signal flips completely with the external magnetic field, which verifies the magnetic origin of the observed THz signal. The inset shows the pump power dependence of the THz amplitude from the same sample. A linear behavior (fit) is observed. **b**, THz emission signals from the AuPt binary alloy series. With varying the Au concentration the amplitude of the THz signal changes in a wide range. **c**, THz transmission signals for sample and reference measurements. **d**, Pump light absorptance plotted as a function of the relative Au concentration.

The inset of Fig. 4.1a shows a linear dependence of the THz signal on the pump power which was varied by usage of a neutral density filter wheel. A linear fit (orange line) is applied to the measured data (blue points). This is consistent with our model for THz emission.

Fig. 4.1b shows the THz emission signals of the entire AuPt-series. We observe a strong dependence of the THz signal on the relative Au concentration $x$. The THz transients of three different samples and their reference from the performed THz transmission measurements are presented in Fig. 4.1c. The reference measurements on the substrate, which was nominally the same for all samples, accord with each other. In contrast the transmitted THz signals through the thin-film stack exhibits a smaller amplitude than the references and, in addition, a difference of the signal amplitudes for different relative Au concentrations is observed.

Panel d in Fig. 4.1 shows the result of the optical absorption measurement. The reflectance $R$ and transmittance $T$ from the sample were measured with a power meter. The absorptance is then given by $A = 1 - R - T$ according to $A + T + R = 1$. Error bars are estimated on the basis of the fluctuations of the measured powers. The pump light absorptance seems to be approximately independent of the Au concentration.

## Conductivities at THz frequencies

The THz transmission measurements provide information on the impedance $Z$ of the bilayer (see chapter 2.7.2). We call the impedance of the entire bilayer $Z_{\text{eff}}$. On top, by using a comparison with theoretical conductivites based on the Drude model, we are able to extract the effective conductivity of the whole thin-film stack. The extraction of the NM layer conductivity becomes possible by using a parallel circuit model where the conductivities of each layer simply sum up based on Kirchhoff's circuit laws.
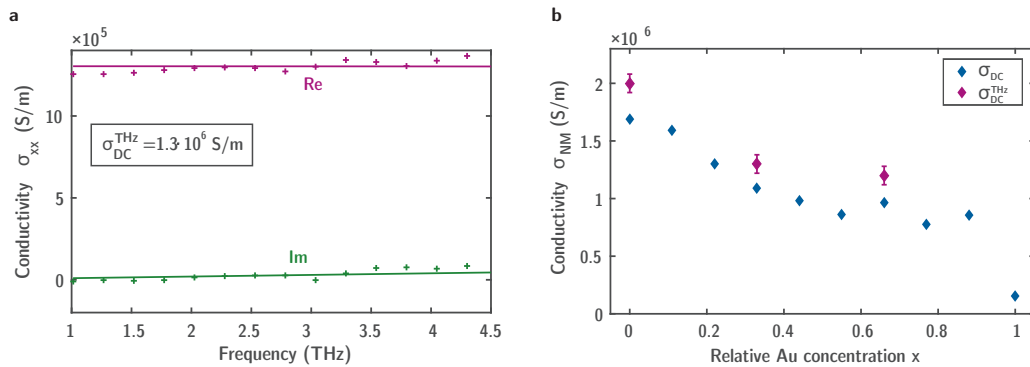


Figure 4.2.: **THz conductivity from Au$_x$Pt$_{1-x}$.** **a**, Conductivity at terahertz frequencies from one typical AuPt sample is shown, imaginary part in green and real part in purple. Both parts are Drude fitted due to the fact, that no extensive frequency dependence can be observed. **b**, THz conductivities from the AuPt series in the dc limit in comparison to dc measurements which were done with a four-point probes method.

Fig. 4.2a shows an example of the extracted the conductivity of one sample in the frequency range between $1\,\text{THz}$ and $4.5\,\text{THz}$. The real part is drawn in purple, the imaginary part in green. Both parts show a linear trend of the conductivity in the measured range. Thus, we perform a Drude fit on both parts and interpolate hereby to the dc regime. Importantly, the imaginary part has to be zero at dc $[\text{Im}\,\sigma(\omega = 0) = 0]$ to fix $\Delta d_{\text{sub}}$ which is satisfied here.

The group of M. Meinert performed conductivity measurements on all samples by using the four-point resistivity method (see chapter 3.2.2). These conductivities $\sigma_{\text{DC}}$ are compared to the conductivites extracted from the THz transmission measurements $\sigma_{\text{DC}}^{\text{THz}}$ in Fig. 4.2b. We learn that $\sigma_{\text{DC}}^{\text{THz}}$ is always slightly higher than $\sigma_{\text{DC}}$, but in the same order of magnitude and it follows clearly the trend. This agreement is remarkable due to two entire different measurement methods in complete different frequency ranges. The typical error of the dc resistivity measurements is estimated in the order of less than $10\,\mu\Omega \cdot \text{cm}$. The observed difference between $\sigma_{\text{DC}}^{\text{THz}}$ and $\sigma_{\text{DC}}$ may be explained by the fact, that $\sigma_{\text{DC}}$ was measured on equivalent, but $40\,\text{nm}$-thick samples, where the bulk conductivity is dominating. By calculating back to $3\,\text{nm}$ thickness, a slight over-estimation of the resistivities could be the result. In contrast, in the thin-film measurements at terahertz frequencies, we are more sensitive to the interface scattering than to the bulk contribution of the conductivity. A model, which describes the conductivity in thin-films is the Fuchs-Sondheimer model and it states that the conductivity of a thin-film is lower than from a bulk sample [Coe02]. Here, the over-estimation of the measured resistivities at dc seems to dominate. But nevertheless, due to the reasonable agreement of $\sigma_{\text{DC}}^{\text{THz}}$ and $\sigma_{\text{DC}}$, the values of $\sigma_{\text{DC}}$ are used for the following evaluation. Moreover, we have to note that not all samples from the AuPt series were measured by THz transmission spectroscopy because it is known from previous experiments that the agreement with electric dc-measurements is quite good. To confirm the previous results, only three samples of this series were measured.

**Contracted raw data**

We have seen the strong dependence of the THz emission waveform amplitudes on $x$ beforehand. To quantify this amplitude variation, we contract the transients to a corresponding mean THz amplitude. A common method is the calculation of the root mean square, but the phase information is lost in this procedure [Bra16a]. We use instead a projection of the THz signal $S$ on a reference waveform $S_{\text{ref}}$, which reads

$$\bar{S} = \frac{1}{N} \langle S_{\text{ref}}, S \rangle = \frac{1}{N} \int \text{d}t\, S_{\text{ref}}(t) S(t) \tag{4.2.1}$$

where $N = \langle S_{\text{ref}}, S_{\text{ref}} \rangle^{1/2}$ is a normalization factor to the reference [Bra16a]. We choose the strongest signal from the set of waveforms in this AuPt series for the reference.
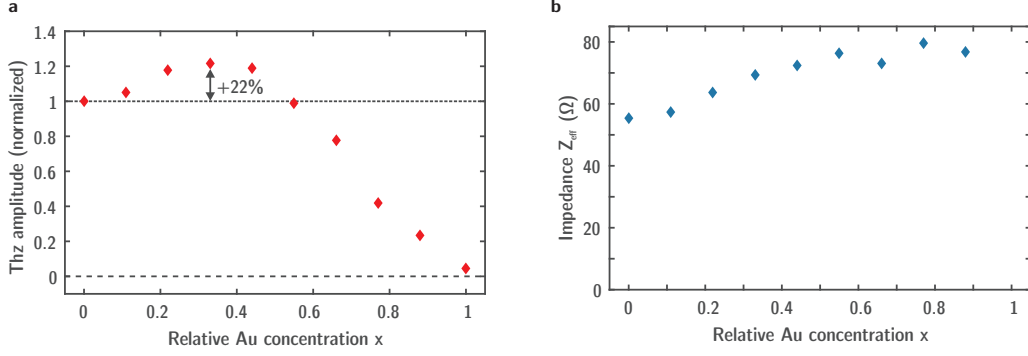
**Figure 4.3.: Contracted raw data from Au$_x$Pt$_{1-x}$. a**, THz emission amplitude. We observe an increase of 22% in the THz signal at a relative Au concentration of 0.33. **b**, Impedance $Z_{\text{eff}}$ extracted from the THz transmission waveforms.

The terahertz amplitude $\bar{S}$ shows a maximum of the THz emission between 30-40 % relative Au concentration and it decreases monotonic up to pure Au above 40 % Au concentration. This complex behavior leads to the question, whether the observed maximum has its origin in a change of spin Hall effect related parameters. According to the THz emission model (see chapter 2.7.1), this trend could also stems from the incoupling efficiency of the pump light ($A$) or/and outcoupling efficiency of the emitted THz electric field ($Z_{\text{eff}}$). We exclude the incoupling, because we noted beforehand that the pump light absorption seems to be independent of $x$ (Fig. 4.1d). The effective impedance, extracted from the THz transmission measurements, is shown in Fig. 4.3b. An impedance change of 30 % in the Pt rich regime is observed. We summarize the influence of pump light absorptance and THz impedance by the coupling function $C(\omega)$ with

$$C(\omega) = \frac{A}{d} \cdot Z_{\text{eff}}(\omega). \tag{4.2.2}$$

**Figure of merit and spin Hall conductivity**

Using $C(\omega)$, we can extract a figure of merit (FoM) that reflects only the intrinsic spintronic parameters of the THz emission:

$$\text{FoM} = \frac{E_{\text{THz}}(\omega)}{C(\omega)} \propto \gamma \cdot \lambda_{\text{rel}} \cdot j_{\text{s}}^0 \cdot \tanh\left(\frac{d_{\text{NM}}}{\lambda_{\text{rel}}}\right) \tag{4.2.3}$$

We used the presented contraction to $\bar{S}$ for the mean of $E_{\text{THz}}(\omega)$ (see above). Fig. 4.4 shows the calculated FoM, where the observed maximum of $\bar{S}$ nearly vanishes. We conclude, that the change in the conductivity seems to be responsible for the maximum THz signal at $\approx 33$ % Au concentration.

To give a trend of the spin Hall conductivity, which is a more fundamental quantity than the spin Hall angle, depending on $x$, there are two parameters still unknown according to equation 4.2.3: $\lambda_{\text{rel}}$ and $j_{\text{s}}^0$. The measurement of $\lambda_{\text{rel}}$ is still missing, because a NM layer thickness variation for each Au concentration is required. The
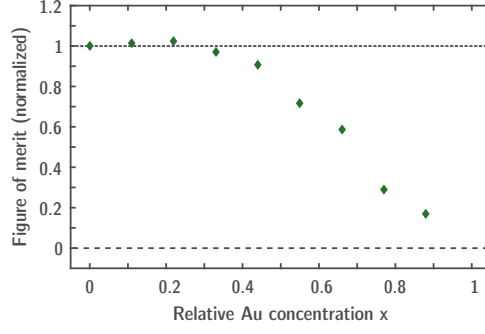
**Figure 4.4.: Figure of merit and spin Hall conductivity from $Au_xPt_{1-x}$.** Figure of merit (FoM) to show the THz signal dependence without incoupling of the pump light and outcoupling of the generated THz electric field. Under the made assumptions the FoM is equivalent to the spin Hall conductivity $\sigma_{SH}$, which shows a change with the composition ratio.

measurement of $\lambda_{rel}$ is a future project, in which the thickness dependence of the NM layer is measured by THz emission. We expect a tanh-like dependence. By fitting a tanh function to the data, where the fit parameter is $\lambda_{rel}$, we obtain $\lambda_{rel}$. To reduce the number of samples, one can sputter a wedge with varying NM thickness. The preparation of such a sample is ongoing.

In contrast to $\lambda_{rel}$, the spin current injected to the NM layer $j_s^0$ is not that easy to measure. In this thesis, we assume firstly, that $j_s^0$ is independent of $x$. In addition, we assume, that the relaxation length $\lambda_{rel}$ is proportional to the Drude time constant $\tau$ (if $d_{NM} \gg \lambda_{rel}$), that is again proportional to the longitudinal conductivity $\sigma_{NM}$.

$$\lambda_{rel} \propto \tau \propto \sigma_{NM} \tag{4.2.4}$$

Furthermore, we assume the charge carriers $n$ to be constant with the relative Au concentration $x$ to justify $\tau \propto \sigma_{NM}$. All these assumptions lead to the ability to calculate a spin Hall conductivity trend. The spin Hall conductivity is defined as

$$\gamma = \frac{\sigma_{SH}}{\sigma_{NM}}. \tag{4.2.5}$$

This yields finally

$$\text{FoM} \propto \gamma \cdot \lambda_{rel} \quad \rightarrow \quad \text{FoM} \propto \frac{\sigma_{SH}}{\sigma_{NM}} \cdot \sigma_{NM} \quad \rightarrow \quad \text{FoM} \propto \sigma_{SH}. \tag{4.2.6}$$

**Discussion**

In conclusion, we note that the figure of merit shows already the trend for the spin Hall conductivity under the made assumptions. Fig. 4.4 shows a monotonic decrease of the spin Hall conductivity from the pure platinum to pure gold regime, which is in good agreement with the findings of Obstbaum *et al.* [Obs16]. We could think of a domination of the skew scattering mechanism in the Pt rich regime, that enhances the longitudinal conductivity $\sigma_{NM}$, whose influence results in a larger THz emission amplitude due to a smaller impedance $Z_{eff}$. Potentially, the dependence of $\sigma_{SH}$ could

have its origin in dominating intrinsic deflection or skew scattering contributions, or a mixture of both. Obstbaum *et al.* simulated the SHE mechanisms at different temperatures and concluded on the basis of a weak temperature dependence of the intrinsic contribution that this mechanism could be the dominating process of the $\sigma_{SH}$ dependence on the relative concentration $x$ [Obs16].

### 4.2.2. Tantalum-gold-alloy $Ta_xAu_{1-x}$

#### Sample preparation

The TaAu layers were dc-magnetron-sputtered at the same pressure and Ar flow as the AuPt samples. A set of twelve binary alloy samples with varying stoichiometry were composed. More details on the sample structure and deposition process are provided in section 3.2.1.

#### Raw data
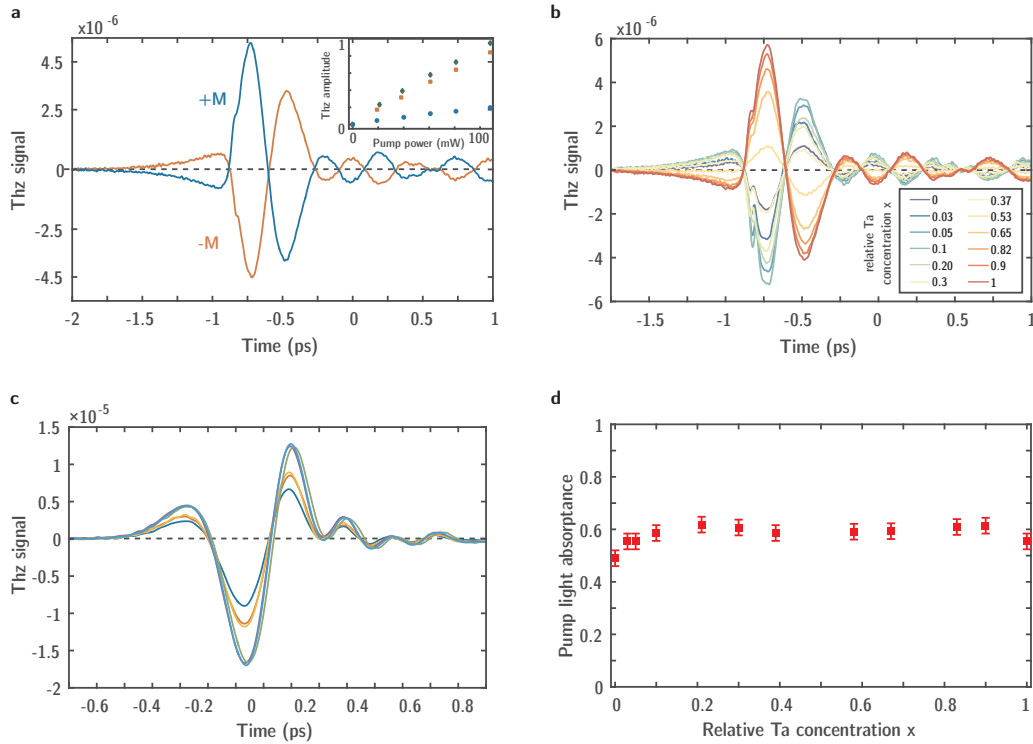


**Figure 4.5.:** **Raw data from $Ta_xAu_{1-x}$. a**, THz signals of one sample from the TaAu series with opposite magnetic field directions (±M). The sign of the THz signal reverses with the magnetic field. Inset: pump power dependence of the THz amplitude from three different sample from the TaAu series. A linear behavior is observed for the tested samples. **b**, THz signals from the TaAu binary alloy series. With varying Ta concentration the amplitude of the THz signal varies in a wide range and changes its sign. **c**, THz transmission signals for samples and reference measurements. **d**, Pump light absorptance plotted as a function of the Ta concentration.

We performed the same measurements as for the AuPt series to characterize the TaAu series: absorption measurements of the optical pump beam, THz emission and

transmission experiments with varying stoichiometry, and for a few samples a check whether the THz emission amplitude goes linearly with the deposited energy of the pump beam.

The THz signal reverses with opposite external magnetic field. A magnetic origin of the signal is given (see Fig. 4.5a). The inset in Fig. 4.5a shows the dependence of the pump power on the THz signals, which was measured for three samples. We observe the expected linear behavior for all tested samples which is in agreement with our THz emission model (described in section 2.7.1). The THz emission raw data in Fig. 4.5b exhibits a strong dependence of the THz signal on varying stoichiometry. To understand the origin of the THz emission signal dependence, pump light absorption and THz transmission measurements are essential. Fig. 4.5c and d show instancing some THz waveforms from the performed THz transmission measurements and respective the optical absorption dependence on $x$. The transmission of THz pulses changes with the Ta concentration $x$ which determines directly a varying impedance of the thin-film layers. The pump light absorption exhibits a small variation on the Ta concentration $x$ in the Au rich regime.

**Contracted raw data**

The recorded THz emission data is contracted in the same way introduced in the previous section by using a referenced projection. This contracted THz amplitude $\bar{S}$ is plotted as a function of $x$ in Fig. 4.6a. A non-trivial relation between THz emission amplitude $\bar{S}$ and the relative Ta concentration $x$ gets visible. In addition, a sign change is observed, which is expected due to a positive spin Hall angle of Au and a negative for Ta [Qu18]. As shown in Fig. 4.6b the impedance $Z_{\text{eff}}$ exhibits a dependence on $x$ below $0.3\%$ relative Ta concentration. This is probably the origin for the increase of the THz amplitude in Fig. 4.6a in the Au rich regime.
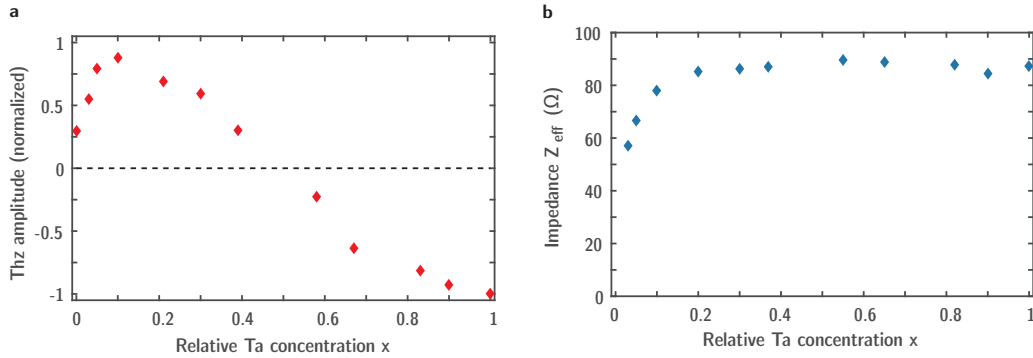


Figure 4.6.: **Contracted raw data from Ta$_x$Au$_{1-x}$. a**, THz emission amplitude. A sign change is observed at 50 % Ta concentration. **b**, Impedance Z$_{\text{eff}}$.

## Figure of merit and spin Hall conductivity

Fig. 4.7a shows the extracted conductivity $\sigma_{\mathrm{NM}}$ of the NM layer. We observe a large conductivity change in the Au rich regime. Above 30 % relative Ta concentration the conductivity stays constant.

Now, we combine our knowledge of the conducted measurements and extract a figure of merit according to equation 4.2.3, which excludes the coupling function and is proportional to the spin-Hall-effect-related parameters (Fig. 4.7b). The FoM shows a decreasing trend with increasing tantalum concentration and the sign change is still observable at $x \approx 50\,\%$ Ta. The coupling function $C(\omega)$ seems to be responsible for the increase of the THz emission signal in the Au rich regime, but seems not to be the main reason for the THz signal dependence shown in Fig. 4.6a.

The relaxation length measurements are also still missing for this series. We make again the same assumptions, mentioned in the previous section, to get a trend for the spin Hall conductivity dependence on $x$. According to equation 4.2.6, the FoM shown on Fig. 4.7b depicts also the trend of the spin Hall conductivity. In the gold rich regime, the spin Hall conductivity decreases rapidly and at 50 % Ta concentration the sign change is still observable.
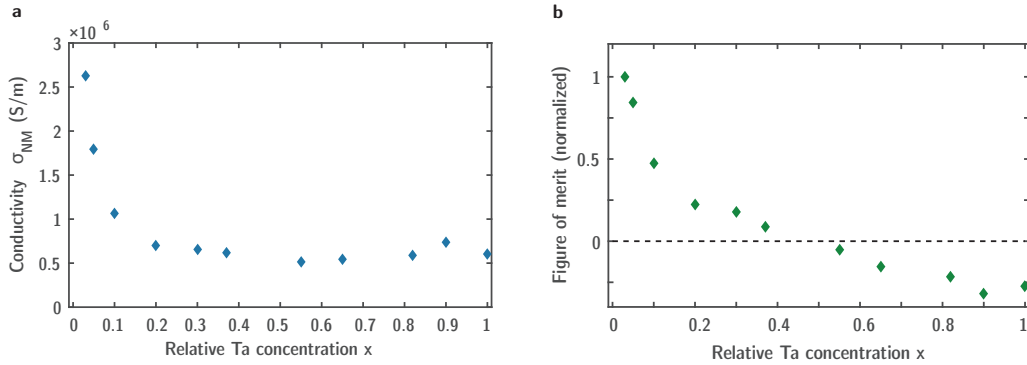


**Figure 4.7.: Longitudinal and spin Hall conductivity from Ta$_x$Au$_{1-x}$. a**, The longitudinal conductivity exhibits a large change in the gold rich regime. Above 30 % Ta incorporation the conductivity stays constant. **b**, The extracted figure of merit (FoM) of the TaAu series as a function of $x$ which shows a decrease with increasing Ta concentration.

## Discussion

The extracted trend of the spin Hall conductivity is in good agreement with Qu *et al.* [Qu18], who recently performed electrical measurements of the the spin Hall effect within the whole concentration range. Furthermore, Qu *et al.* suggests that the intrinsic contribution plays the major role in the spin Hall effect in TaAu based on first-principle calculations [Qu18]. In addition, Laczkowski *et al.* claimed that especially in the Au-rich regime the Ta impurities lead to a dominant contribution of the side-jump-scattering [Lac17].

Our experimental results can support possibly both theories due to the similar trend of

the spin Hall conductivity and respective the impedance change in the Au rich regime.

Quite recently resistivity and x-ray reflectivity measurements (see appendix A.3), conducted by Satya Prakash Bommanaboyena from the university of Bielefeld, showed that the studied samples with a layer thickness of 3 nm dominated by a gold concentration are extremely rough at the CoFeB|TaAu interface due to the tendency of Au to form islands, when grown on fused silica. On the one hand, the films need to be thick enough so that the islands coalesce and form a relatively smooth film, which is not suitable for THz emission on the other hand. A solution to overcome this trade-off could be the reversal of the stacking order by depositing the binary alloy TaAu on top of the FM layer. The final sample structure would look like: substrate || CoFeB | TaAu.
This mentioned roughness may explain the change in the impedance and THz amplitude in the Au rich regime (see Fig. 4.6a).

### 4.2.3. Comparison to electrical measurements

To evaluate whether THz emission is a suitable technique to characterize the spin Hall effect in spintronic-relevant materials, we compare the results of the beforehand presented material systems with the results from two different electrical methods. For this purpose, we collaborated with the group of Markus Meinert from the university of Bielefeld, who performed harmonic Hall measurements at kHz frequencies and with Mathias Weiler from the Walter-Meißner-Institute, who characterized the materials by an inductive spin pumping method in the GHz range.

#### Harmonic Hall technique

The working principle of the harmonic Hall technique is described in detail in section 2.6.3. The performed measurements were done by applying an ac in-plane current with a frequency of 3.219 kHz along the Hall bar structure (see Fig. 2.6b). The in-plane magnetic field was varied from -1.6 T to 1.6 T and a lock-in amplifier was used to measure the Hall-voltages. The evaluation is based on the method presented in [Wen17].

#### Inductive spin pumping

The inductive spin pumping method measures electrically the spin Hall effect, but here no pattering/microstructuring is needed. Basic information about spin pumping and its usage to measure the SHE can be found in the sections 2.4.1 and 2.6.1. A microwave field (rf, radio frequency) generated by a vector network analyzer (VNA) induces a spin precession at the ferromagnetic resonance inside the sample. The rf field pumps spin current by spin pumping which is transformed by the spin Hall effect into a transverse charge current. This charge currents retroacts to the driving

microwave field, which is transmitted through the sample. The VNA is used as a detector to measure phase-sensitive the transmitted microwave field. Here, only field-swept measurements were performed, which means that the VNA-frequency is fixed and the out-of-plane magnetic field (up to $3\,\mathrm{T}$) is swept through the magnetic resonance. By analyzing symmetries of the measured signals, it becomes possible to isolate spin Hall effect parameters such as the spin Hall angle. Please see [Ber17] for more information about the extraction of spin Hall parameters from the measured transmission parameter.

### Ab-initio calculations

In addition, we use ab-initio calculations for this comparison. We use the theory data for AuPt from Obstbaum *et al.* [Obs16]. Calculations on the TaAu series are provided by Sebastian Wimmer from the LMU Munich. All ab-initio data is calculated with a spin polarized relativistic Korringa-Kohn-Rostoker (SPRKKR) code which is based on a Dirac-Hamiltonian for a spin-polarized system [Ebe17]. This code uses Kubos linear response formalism and calculates the underlying electronic structure, and intrinsic and extrinsic contributions with the Korringa-Kohn-Rostoker Green function method [Obs16].

### Comparison of the methods
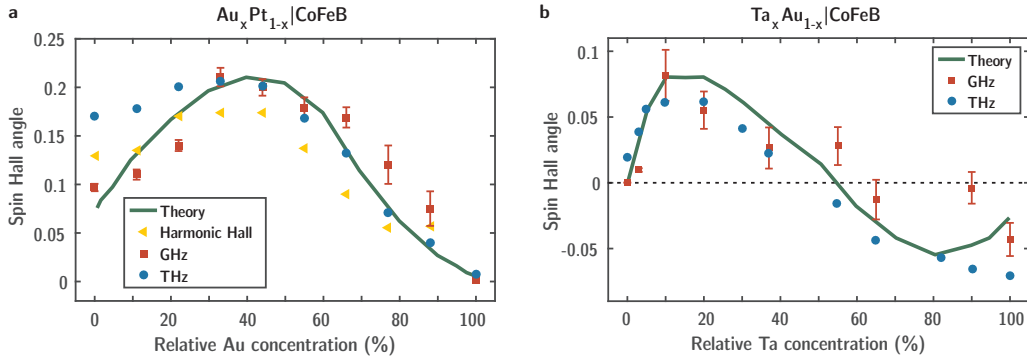


Figure 4.8.: **Comparison of the spin Hall angles from binary alloys measured with three different methods**, Spin Hall angle of the **a** AuPt series and **b** TaAu series measured with the Harmonic Hall method, the inductive spin pumping technique, and terahertz emission spectroscopy. Ab-initio calculations are shown as a green line.

Fig. 4.8 shows the spin Hall angle of the a) AuPt and b) TaAu series for the three methods and ab-initio calculations (green line). For the TaAu series, there is no harmonic Hall data available, the big roughness in the gold rich regime inhibited such measurements.

We observe a good agreement concerning the trend of the spin Hall angle for all methods and both material systems. Their key features such as the sign change in the TaAu series are always visible.

Here we have to mention that spin pumping and harmonic Hall technique are quantitative methods which deliver absolute values of e.g. the spin Hall angle. In contrast, the THz emission measurements are semi-quantitative as the signal magnitudes have to be compared to a reference [Lie17]. To match the contracted THz amplitude to the theory data, an arbitrary factor was chosen. We conclude, that the contracted THz amplitude $\bar{S}$ seems to be directly proportional to $\gamma \cdot \lambda_{\mathrm{rel}}$.

In summary, three completely different measurement techniques in various frequency ranges were used to study binary alloys with respect to their spin-Hall-effect parameters with varying relative concentration and all techniques provide the same trend for the spin Hall angle. This shows, that THz emission spectroscopy is a good, alternative method with certain advantages compared to common electrical methods, to characterize spintronic-relevant materials.

## 4.3. Oxygen doped $\beta$-tungsten WO$_x$

### Motivation

Ferromagnetic resonance measurements have shown that oxygen-doped $\beta$-W exhibits an enhanced spin Hall effect [Dem16]. By adding oxygen to pure W, the so called $\beta$-phase (A15 cubic phase) of W is stabilized [Dem16]. This leads to the question of how the spin Hall angle $\gamma$ and the $E_{\mathrm{THz}}$ depend on the oxygen content. By using our all-optical method of THz emission spectroscopy, we are able to rapidly screen a set of $\beta$-W samples with varying oxygen doping.

### Sample preparation

Some more information on the $\beta$-W samples is given here. They are dc-magnetron-sputtered with an Ar:O$_2$ flow-rate ratio in the working gas of 40:0.2. The $\alpha$-W sample was sputtered under a pure Ar atmosphere with a flow of $10\,\mathrm{sccm}$. All samples were sputtered with a pressure of $3 \cdot 10^{-3}\,\mathrm{mbar}$ and a deposition rate of $0.013\,\mathrm{\AA/Ws}$. By tuning the sputtering power, the oxygen incorporation is controlled. A lower sputtering power gives a higher oxygen content.

### Raw data

A reversal of the THz waveform sign is observed for opposite external magnetic fields (Fig. 4.9a). As shown typically in the inset of Fig. 4.9a all of the samples exhibits a linear dependence on the pump power. Both observations identify the origin of the signal to be magnetic and consistent with the inverse spin Hall effect scenario for THz emission. Fig. 4.9b shows the THz emission waveforms with varying oxygen content $x$. A strong dependence on $x$ of the signal is observed. The THz transmission (Fig. 4.9c) and pump light absorptance measurements (Fig. 4.9d) were performed to study the influence of the coupling function $C(\omega)$ on the THz signal shown in Fig.

4.9b. The optical absorptance exhibits no big dependence as a function of the inverse sputtering power, which is proportional to the incorporated oxygen content.
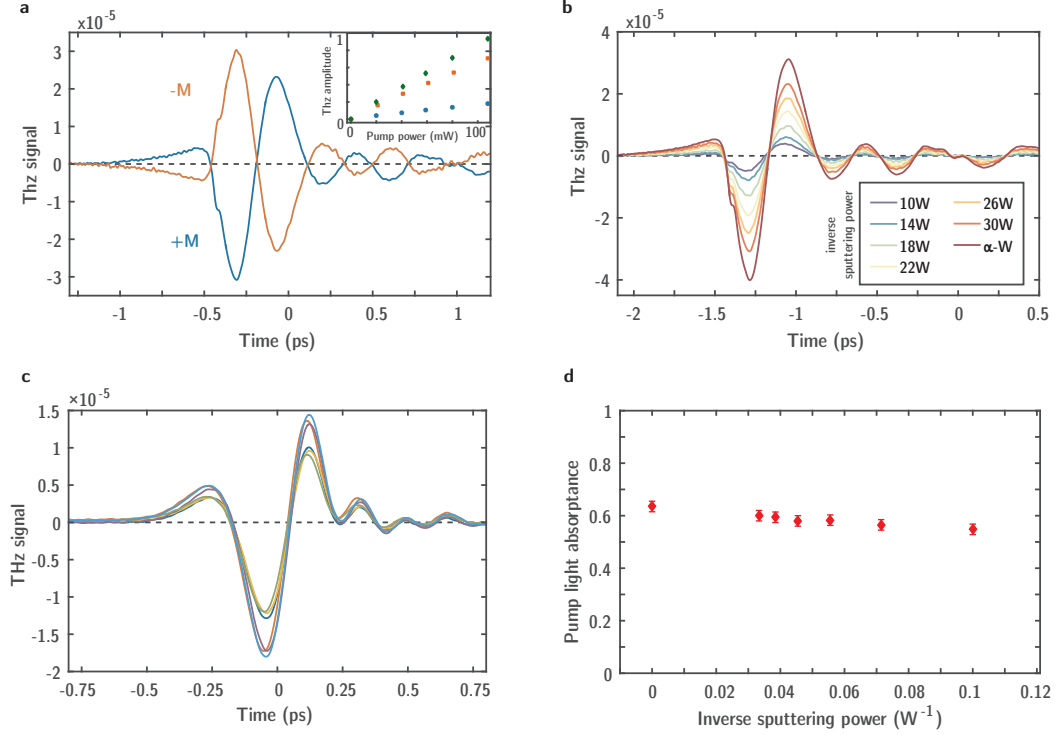


Figure 4.9.: **Raw data from the oxygen doped $\beta$-tungsten series.** **a**, THz signals with opposite magnetic-field directions ($\pm$M). The THz signal reverses completely with the external magnetic field. Inset: pump power dependence of the THz amplitude from three different WO$_x$ samples. A linear behavior is observed for all of them. **b**, THz emission signals. By adding oxygen to the system, the signal decreases. **c**, THz transmission signals. **d**, Pump light absorptance.

## Contracted raw data

By using the introduced contraction of an THz transient to a mean THz amplitude $\bar{S}$, Fig. 4.10a shows $\bar{S}$, which decreases with increasing oxygen content. The highest signal is observed from the control sample without any oxygen doping, called $\alpha$-W sample, which is not expected due to the predicted enhancement of the spin-to-charge conversion in $\beta$-W.

Fig. 4.10b shows the impedance of the WO$_x$ series. We consider only the $\beta$-phase samples, because the $\alpha$-phase is not part of the interesting regime. Due to the frequency independence of the conductivity and the good agreement between $\sigma_{\mathrm{DC}}$ and exemplary measured $\sigma_{\mathrm{DC}}^{\mathrm{THz}}$, we use again dc conductivities provided my M. Meinert's group. We note that there is no big dependence of the impedance on the oxygen content $x$. We conclude, that either the impedance nor the pump light absorptance are responsible for the strong oxygen dependence of the THz signal.
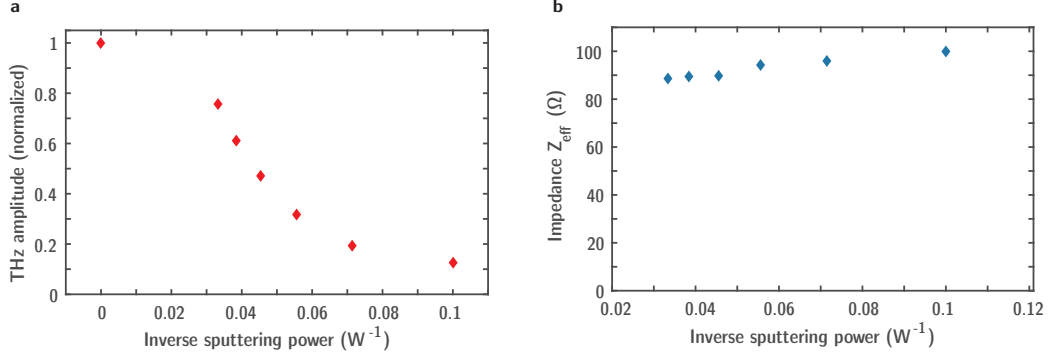
**Figure 4.10.:** **Contracted raw data from oxygen doped $\beta$-tungsten.** **a**, THz emission amplitude. We observe a decrease THz amplitude with increasing oxygen doping. **b**, Impedance $Z_{\mathrm{eff}}$.

## Figure of merit and spin Hall conductivity

In addition to the impedance shown in Fig. 4.10b, Fig. 4.11a shows the conductivity of the NM layer, which decreases with increasing oxygen content.

To verify that the coupling function is indeed not the reason for the varying THz signal, we calculate the figure of merit (see Eq. 4.2.3). The FoM shown in Fig. 4.11b shows that the THz signal variation with oxygen content is directly related to the inverse spin Hall effect, because the trend persists when excluding $C(\omega)$.

Due to missing measurements of $\lambda_{\mathrm{rel}}$, we assume again that the relaxation length $\lambda_{\mathrm{rel}}$ scales proportional to the longitudinal conductivity and $n$ is independent of the doping content $x$. In addition, we again have to assume the independence of $j_{\mathrm{s}}^0$ on $x$. This leads to the known proportionality between the FoM and the spin Hall conductivity (see Eq. 4.2.6) depicted in Fig. 4.11b. The oxygen doping modifies the spin Hall conductivity, which results in a monotonic decrease of $\sigma_{\mathrm{SH}}$ with increasing oxygen content.



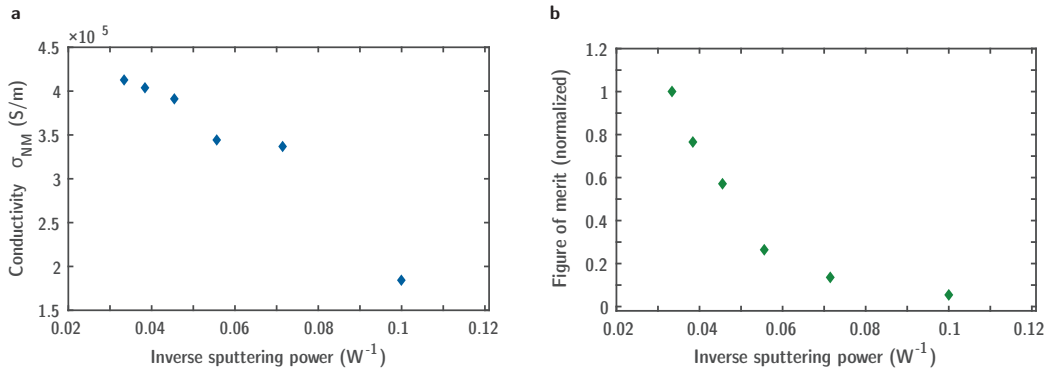**Figure 4.11.:** **Conductivity and Spin Hall conductivity from the oxygen doped $\beta$-tungsten series.** **a**, Longitudinal conductivity of the NM layer. A decreasing trnd with increasing oxygen doping is observed. **b**, Figure of merit, normalized to the most efficient sample, of the $WO_x$ series as a function of the inverse sputtering power. It is clearly a decreasing trend with increasing oxygen content visible.

**Discussion**

The reason for this modification is only speculative. One may think of an enhancement of the extrinsic contributions due to the oxygen impurities or *Demasius et al.* [Dem16] suggests a scenario, where interfacial spin-orbit-torques are responsible for the observed dependence. We have to note that in contrast to Demasius *et al.* [Dem16], Mondal *et al.* achieved the $\beta$-phase of W by thickness variation of the W layer [Mon17]. They studied CoFeB|W samples and their resistivity changes by time-resolved MOKE and demonstrated a stable $\beta$-phase below 5 nm W thickness. Following this observations, all of our samples with 3 nm W layers, including the $\alpha$-W sample, should be in the $\beta$-phase. At the moment, it is not clear whether a stable $\beta$-phase of W is always realized in samples with a W thickness such as 3 nm we were using or whether the sample preparation is crucial.

Additional to this ambiguity, X-ray reflectivity measurements, recently performed by Satya Prakash Bommanaboyena, revealed that our tungsten layers are probably highly over oxidized due to the stacking order and the used substrate. The W layer is deposited directly on top of the fused silica ($SiO_2$) substrate. We think, that oxygen from the substrate could be diffused into the W, which results in over-oxidized W layers. To test this theory, M. Meinert will reverse the stacking order to substrate || CoFeB (3 nm) | $WO_x$ (3 nm) | Si (1.5 nm) and deposit the thin-film stack on a native Si substrate.

## 4.4. Summary and outlook

**Summary**

By comparing our THz amplitudes $\bar{S}$ to other methods, we revealed that THz emission spectroscopy directly monitors the relative strength in the inverse spin Hall effect relative to a reference sample. The other methods need a much more complicate evaluation of the data to show changes and trends in the SHE. The advantage of these electrical methods is that they are able to provide absolute values, e.g. for the spin Hall angle compared to THz emission measurements. But THz emission is a fast and contact-free characterization tool for thin, high-spin-orbit materials. We are able to identify, whether a signal dependence stems from optical in- or THz out-coupling or stems from changes in the ISHE.

Studying the AuPt series, we observed an enhancement of the THz signal in the platinum rich regime, which has its origin in a conductivity change, that is suitable for THz out coupling in this specific case. However, changes in the SHE parameters are responsible for the smooth THz signal dependence with varying Au concentration. We revealed, that the TaAu series shows the expected sign change which is observed at 50 % Ta concentration. Likewise, the THz signal change stems from spin Hall effects related parameters.

The last studied material system, $WO_x$, showed a THz signal dependence, which stems from spin Hall effect related parameters. But the $\alpha$-phase sample was the most efficient one due to the stacking order and linked over-oxidation of the W layer.

**Outlook**

We will measure the reversed stack sequence of the $WO_x$ and TaAu series by THz emission spectroscopy to avoid the mentioned issues of the samples. A characterization of other highly promising compounds and alloys will be another future project and we would like to try to implement the best AuPt concentration, and maybe an improved W ($WO_x$), for a new generation of spintronic terahertz emitters.

# 5. Measuring magnetic hysteresis by THz emission

## 5.1. Motivation

This chapter is motivated by a first test of the electromagnet (see chapter 3.3.1) in the dc mode. For this purpose, we use our standard tool of terahertz emission spectroscopy to measure magnetic hysteresis loops of thin metallic films with high spin-orbit-coupling at a good signal-to-noise ratio (SNR). We want to test whether THz emission is a suitable tool to measure hysteresis loops. For comparison, we measure the hysteresis loops with a common method, the magneto-optic Faraday effect.

## 5.2. Magnetic hysteresis loops from CoFeB/Pt bilayers

### 5.2.1. Experimental setup

We use the terahertz emission setup with the electro-optic detection described in section 3.1.4. To vary the magnetic field, we use the electromagnet introduced in section 3.3.1. The electromagnet is tilted roughly by $40°$ from our standard angle of incidence. This angle is the maximum, we could realize due to the geometry of the electromagnet. In principle, higher angles would be appreciated for the Faraday signal, because one can increase the projection of the in-plane magnetization. In contrast, by tilting the magnet system and the sample respective, we decrease the THz emission amplitude, which is dominated by an out-of-plane spin current. The electromagnet is driven by a Kepco *BOP20-20M* bipolar power supply which provides up to $20\,A$ dc current and allows to sweep the current from the negative to the positive regime. We calibrate the magnetic field strength at the sample position depending on the applied current by using a Hall probe. The additional integrated components for Faraday signal detection are depicted in Fig. 3.8. The data acquisition is realized with a lock-in amplifier *SR830* from Stanford Research Systems.

We studied metallic thin-film samples with varying the Pt thickness and vary additionally the thickness of CoFeB by holding the Pt layer thickness constant. In detail, the samples structures are glass $(500\,\mu m)\,\|\,Co_{40}Fe_{40}B_{20}\,(3\,nm)\,|\,Pt\,(x\,nm)$ with $x = 2, 4, 6, 10, 16$ and glass $(500\,\mu m)\,\|\,Co_{40}Fe_{40}B_{20}\,(y\,nm)\,|\,Pt\,(2\,nm)$ with $y = 5, 10, 20$. We sample each hysteresis loop with $60$ points in the THz and Faraday measurements. For the THz emission experiment we swept once through the hysteresis. In contrast, the Faraday measurements were performed with roughly $100$ iterations through the loop to get a good SNR.
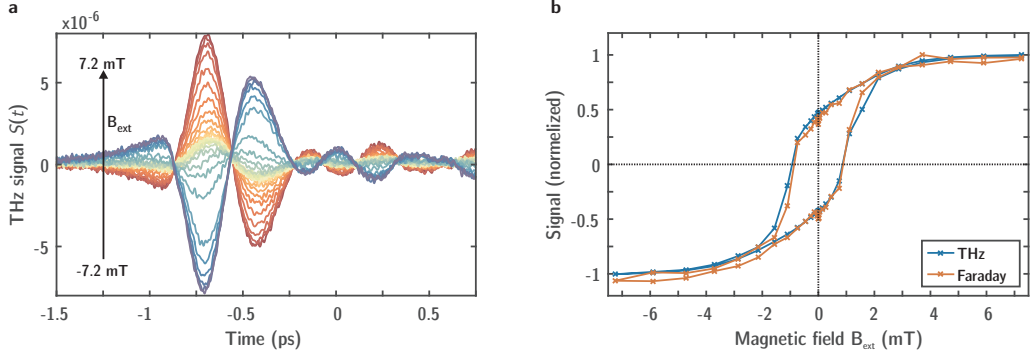
**Figure 5.1.: Magnetic hysteresis loops from CoFeB (3 nm) | Pt (6 nm). a**, THz raw signals for one half sweep of the hysteresis loop. **b**, THz amplitude in comparison with the Faraday signal. The hysteresis loops have an identical shape.

## 5.2.2. Results: THz emission vs optical Faraday effect

Fig. 5.1a shows an example of THz emission raw data for a half hysteresis with sweeping the magnetic field from -7.2 mT (blue) to +7.2 mT (red). We see a strong dependence of the THz signal on the strength of the magnetic field.

By using our standard approach to contract THz waveforms to a mean THz amplitude $\bar{S}$ (see chapter 4.2.1), we get the dependence on the external magnetic field (see Fig. 5.1b). We notice that the terahertz hysteresis loop is similarly shaped compared to the Faraday hysteresis. Furthermore, THz and Faraday measurements exhibit the same coercive fields. The saturation magnetization is also comparable for both methods, but for example the bottom branch in Fig. 5.1b shows a slight difference. This can be caused in phase shifts of the THz signals. In addition, a Faraday effect in the substrate can produce such a difference between THz and Faraday signals.

Not shown are the seven other measured hysteresis loops because they all exhibit the same shape for Faraday measurements and THz emission ones. However, we realized that the general shape of the hysteresis loops changes. Fig. 5.2 shows two hysteresis loops measured on the same sample by THz emission. The varying parameter is the azimuthal rotation of the sample. In addition, a difference in the coercive fields
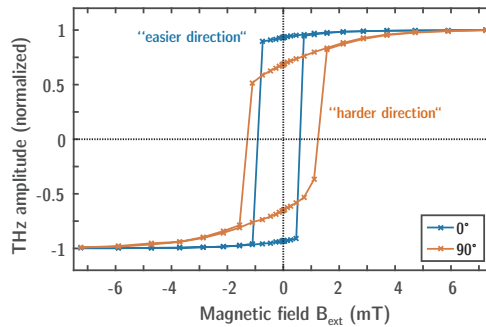


**Figure 5.2.: Magnetic hysteresis loops from different sample orientations.** Magnetic hysteresis loops from a CoFeB (3 nm)|Pt (2 nm) sample. By azimuthal rotation of the sample by 90°, two different anisotropy axes are observed.

is observed. This behavior can be explained by the fact that the sample exhibits an in-plane anisotropy, where the magnetization prefers one axis. For alignments of the external field close to parallel to the e.g. easy axis, we see as expected a more rectangular shaped hysteresis [Tan08].

### 5.2.3. Conclusion

We measured magnetic hysteresis loops by THz emission six times faster than the Faraday measurements. In addition, we achieved a better signal-to-noise ration with THz measurements during these measurement duration. We note, however, that for the measurement of Faraday signals no femtosecond lasers are needed, which makes this technique more universal for many labs. However, our comparison of terahertz and Faraday signals shows that terahertz emission spectroscopy is a beneficial alternative to e.g. time-resolved MOKE experiments.
When dealing with thin-films, magneto-optical signals are getting smaller than in bulk-samples. This results in longer averaging times to get a good signal-to-noise ratio. In contrast, THz emission increases with decreasing film thickness and permits thereby shorter measurement durations.
In summary, THz emission spectroscopy is a suitable alternative to measure magnetic hysteresis loops when dealing with thin-films compared to standard techniques using magneto-optical effects. In principle, we think that THz emission is mostly sensitive to interface effects, which indicates that surface regions exhibit hysteresis very similar to bulk FM. However we seem to be able to measure a bulk property like magnetic hysteresis loops. This result opens up new questions about the THz emission underlying physics which have to be discussed and experimentally explored in the future.

# 6. Outlook: polarization modulation of the spintronic terahertz emitter

This chapter should give an outlook on future experimental work with the electro-magnet system introduced in section 3.3.1. After successful testing the dc mode in the previous chapter, here, we use the electromagnet to produce a rotating THz polarization by applying a sine with a certain frequency to one coil pair and a cosine to the other pair with the same frequency (see Fig. 6.1a). This procedure leads to a rotating in-plane magnetic field (see Fig. 6.1b) because the transverse charge current $j_c$ is always perpendicular to the magnetic field. We expect the magnetization to follow the external field, which enables the modulation of the THz polarization plane.
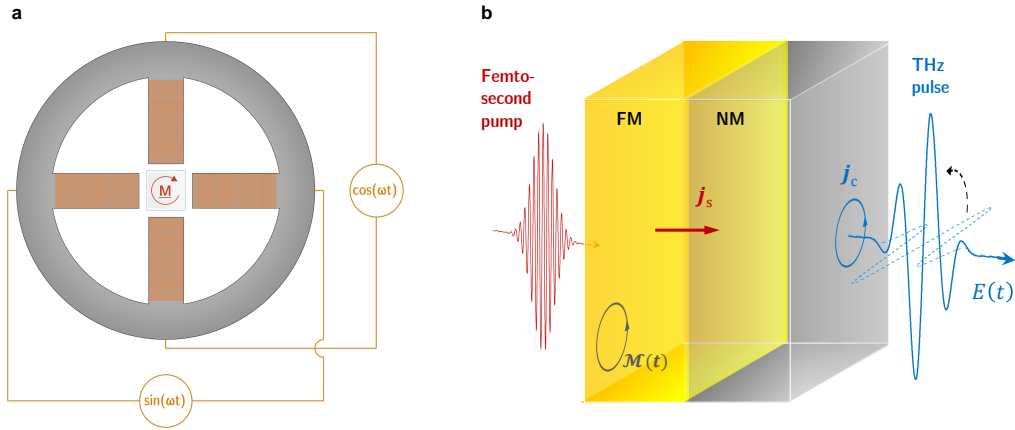


**Figure 6.1.: Modulation of the spintronic terahertz emitter.** **a**, Schematic of the electromagnet shape. Sinusiodal and cosinusiodal ac currents are applied to rotate the magnetic field at the sample position and thereby rotating the sample magnetization. **b**, THz emission scheme to illustrate the consequences of a rotating magnetization inside the FM layer. The charge current $j_c$ also rotates and finally the linear polarization plane of subsequent pulses can be rotated with the frequency of the external magnetic field.

## 6.1. Rotating the magnetization of a thin-film bilayer

For this measurements, we use a CoFeB (3 nm) | Pt (2 nm) sample on glass (500 µm) and measure in the same geometry with integrated Faraday setup as described in the previous chapter. Here, a 2-channel frequency generator drives a 2-channel amplifier which delivers up to 3 A ac current to each solenoid pair of the electromagnet system. By introducing a rotating magnetic field, we add another modulation to our signal. To make it less complicated, we fixed the shaker mechanically at a certain position/time delay and switched off the optical chopper. By using the lock-in amplifier SR830, we demodulate our signal with the frequency of the applied ac currents. The data is recorded by an oscilloscope. In these experiments, we illuminate the sample under
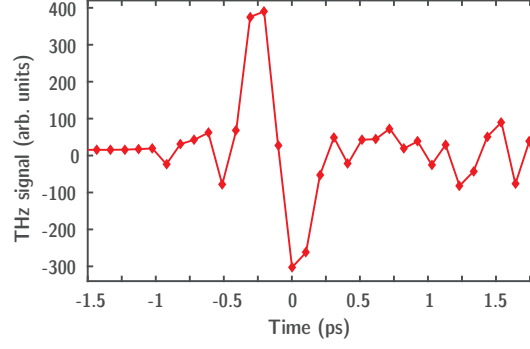
**Figure 6.2.: Terahertz waveform**. Recorded in step-scan mode with a linear translation stage. The measurements with rotating magnetic field were done at the maximum amplitude of the terahertz signal.

normal incidence.

To confirm that we still record THz signals, we measured a THz transient in a step-scan procedure. For this time-resolved measurement we varied manually the time delay in steps of 30 µm with a linear translation stage. Fig. 6.2 shows clearly a waveform.

For all of the following THz measurements with rotating magnetic fields, we reside on the maximum of the THZ signal to obtain the best signal-to-noise ratio. With the oscilloscope we displayed the time evolution of the rotating magnetic field, measured by a Hall probe, and the THz signal. Similar to the hysteresis loops, we measure additionally Faraday signals. To verify the Faraday signal, we measured in dc conditions under normal incidence and got as expected no signal, because the magnetization is completely in-plane and thus the Faraday effect is not working. But in the ac mode, Faraday signals are visible due to an out-of-plane canting of the magnetization, which is possible according to the Landau-Lifshitz-Gilbert (LLG) equation.

## Magnetic field at 10 Hz

We set a frequency of 10 Hz for the driving magnetic field. As shown in Fig. 6.3a (top panel), the THz signal (blue) is able to follow the external field (orange). The magnetic field is monitored simultaneously to the THz/Faraday measurements by a Hall probe in the ac mode. However the Faraday signal shows the same behavior as the THz signal, but the Faraday signal is not stable with respect to its amplitude (Fig. 6.3a (bottom panel)). We believe, that this amplitude instability has its reason in the weak SNR of the Faraday signal. In summary, we conclude that at 10 Hz the magnetization inside the sample is able to follow the driving external field.

## Magnetic field at higher frequencies

We tried to push the ac operation to higher frequencies, starting with several hundreds of Hz. Hereby, we found an interesting, but not expected behavior. Above 100 Hz,
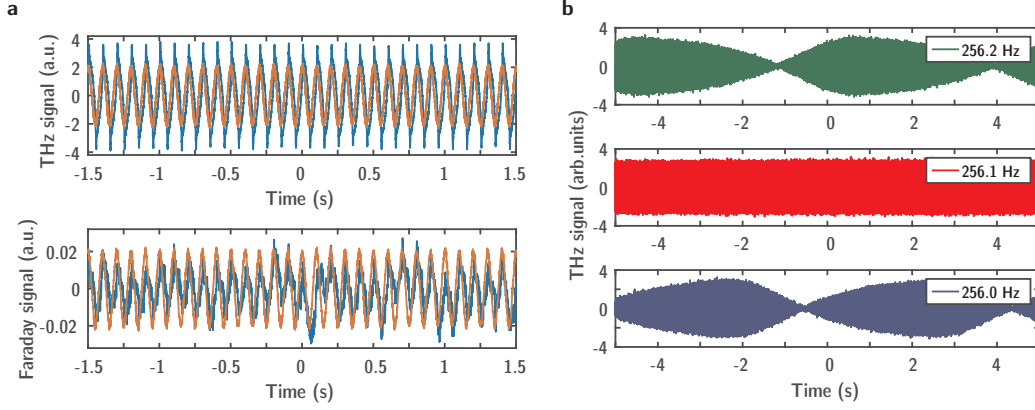
**Figure 6.3.: Modulated THz field at different frequencies**. **a**, Signals recorded at 10 Hz modulation frequency of the magnetic field. Magnetic field measured by a Hall probe in the ac mode are shown in orange, signals in blue. The THz signal follows clearly the driving magnetic field as the Faraday signal, but amplitude variations are observable in the Faraday signal. **b**, THz signals modulated at 256.0 Hz, 256.1 Hz and 256.2 Hz. A long time amplitude-stable signal is observed only at 256.1 Hz (red). Detuning the driving field from this frequency results in an additional beating with a difference frequency to 256.1 Hz.

the amplitude of both signals, THz emission and Faraday, is not stable anymore. An additional beating appears on top of the signal. By sweeping through the frequencies we identified 256.1 Hz the only frequency without an amplitude variation in time (see Fig. 6.3b - middle panel). By slightly detuning the frequency of $\pm 0.1$ Hz from 256.1 Hz, the beating becomes visible. We identify the beating frequency to be the difference frequency between 256.1 Hz and the current frequency. Indeed, the description of the magnetization dynamics is given by the highly nonlinear LLG equation [Sto06]

$$\frac{\mathrm{d}\boldsymbol{M}}{\mathrm{d}t} = \gamma\left[\boldsymbol{m} \times \boldsymbol{H}\right] + \frac{\alpha}{M}\left[\boldsymbol{M} \times \frac{\mathrm{d}\boldsymbol{M}}{\mathrm{d}t}\right], \tag{6.1.1}$$

which contains a damping term $\alpha\left[\boldsymbol{M} \times \dot{\boldsymbol{M}}\right]$, that can principally produce terms where frequencies can be mixed. But nevertheless, it is not fully clear what happens here.

At higher frequencies than $\sim 256$ Hz, the magnetic field was obviously too weak to saturate the sample due to losses inside the ferrite core, which are increasing with increasing frequency. This probably effects negatively the whole system that above $\sim 256$ Hz the magnetization cannot follow the driving field anymore under the used experimental conditions. We confirmed this theory only in the point that indeed the magnetization seems not to be able to follow the external field anymore. All these statements are not necessarily general conclusions. It needs further experiments to exclude probable influences of the electromagnet and measurement electronics.

## 6.2. Next steps: simulation and optimization

In the future, we will optimize of the electromagnet geometry to enhance the magnetic field. By increasing the field strength, we hope to exclude effects on not fully saturated samples. In addition, we need to increase the capability of the amplifier to provide higher ac currents. The third project will be a simulation of the magnetization dynamics in the case of a rotating magnetic field by solving the Landau-Lifshitz-Gilbert equation. Furthermore, we have to clarify, whether a cross talk of the two coil pairs has an influence on the results or whether the cross talk only lowers the magnetic field strength.

# 7. Summary

## Characterization of spintronic materials

We showed that terahertz emission spectroscopy is a suitable tool to characterize spintronic-relevant materials with respect to their spin-to-charge conversion efficiency. In particular, our all-optical method exhibits several advantages compared to electrical SHE measurement techniques, which are commonly used. THz emission measurements are contact-free and do not require a time- and cost-consuming microstructuring.

We characterized three different high-promising material systems: two binary alloys and one doped metal system. A AuPt alloy with varying stoichiometry was studied by THz emission spectroscopy. We observed an increase of $22\,\%$ of the THz emssion in the Pt rich regime and a smooth mean amplitude variation up to pure Au. By measuring the coupling function (optical in- and THz out-coupling) we revealed that this increases stems from a change in the THz out-coupling. Based on some assumptions a trend of the spin Hall conductivity vs. the Au concentration $x$ was calculated. This trend is monotonic decreasing from pure Pt to pure Au and is in good agreement with studies from other groups.

In the second binary alloy TaAu, we varied the relative Ta concentration from zero to one. Our THz emission measurements show a sign change at $\sim 50\,\%$ Ta concentration. Further experiments revealed that this sign change is likely related to a monotonic change in the spin Hall conductivity. An increase of the THz emission signal in the Au rich regime turned out to be related to an impedance change. Again, our results are in good agreement with published studies of other groups. However, to exclude a possible impact of a rough Au surface, we will soon measure again for a reversed stacking order.

The last material system studied in this thesis, is oxygen doped tungsten. By doping pure tungsten the so-called $\beta$-phase of tungsten should get stabilized and exhibit a higher spin-orbit coupling that could result in a more efficient spin-to-charge conversion. We measured this system by THz emission with varying oxygen doping to find the best doping content. However, the control sample, pure tungsten, showed the highest signal. The $\beta$-samples showed a decreasing trend in the spin Hall conductivity with increasing oxygen content. We think that our samples were highly over-oxidized due to the stacking order. An improved sample series will be measured in the near future.

For all three material systems, the measurements of the spin relaxation length is still missing. We assumed it to be proportional to the longitudinal conductivity of the NM layer. Future experiments measuring this relaxation length will be done to verify our assumption.

By comparing our results from the binary alloy series to two absolutely different SHE measurement methods, we revealed that our technique monitors directly changes in the ISHE. In addition, the compared methods are working on different frequency scales. They covered a range from the kHz to the GHz regime and our measurements extended the SHE measurement on the binary alloys to the THz regime. The good agreement of the results of all methods shows that the measurement of the spin-to-charge conversion via the spin Hall effect in spintronic-interesting FM|NM structures does not depend on the measurement frequency. However, the THz emission spectroscopy is a semi-quantitative method that requires a reference measurement from a well-known sample.

**Hysteresis measurement and magnetization rotation**

We developed a quadrupole electromagnet to generate contact-free in-plane magnetic fields. We designed the system in a way that we are able to switch between two different in-plane magnetization directions perpendicular to each other. In addition, by applying ac currents to the electromagnet coils, we enabled an operation mode for a rotating in-plane magnetic field.

We tested the electromagnet in the dc mode by measuring magnetic hysteresis loops of thin-film samples. We compared two different measurement approaches. First, we used THz emission spectroscopy and second, we measured the hysteresis loops by the common magneto-optical Faraday effect. The hysteresis shapes and coercive fields of all studied CoFeB|Pt thin film samples coincide for both techniques. In addition, we were able to distinguish between different anisotropy axes of the samples due to different hysteresis shapes by azimuthal rotation of the samples. We conclude that THz emission is a suitable alternative to measure hysteresis loops. For spintronic-relevant thin-film samples we were even six times faster to obtain a comparable signal-to-noise ratio than the Faraday technique.

At last, we used the electromagnet is the ac mode. By applying, respectively, a sinusoidal and cosinusoidal ac current to the coils, we rotated the magnetic field in-plane and attempted to modulate the polarization plane of the emitted THz electric field. For low frequencies ($< 100\,\text{Hz}$), we observed that the magnetization inside the sample was able to follow the driving external field. Above 100 Hz, however, we saw an additional slow beating on top of the signal amplitude, which turned out to oscillate at the difference frequency to 256.1 Hz. At the latter frequency, the beating vanishes and far above this frequency the magnetization was not able to follow the magnetic field anymore. To better understand this behavior, simulations of the magnetization dynamics are currently underway.

# A. Appendix

## A.1. THz emission model

To derive the THz emission model from scratch, we have to solve the wave equation in the frequency domain

$$\left[\partial_z^2 + k^2(z,\omega)\right] E(z,\omega) = -\frac{e}{ic} Z_0 \omega \cdot j_c(z,\omega) \tag{A.1.1}$$

Here, we assume that the beam diameter of the optical pulse is much bigger than the sample thickness. This justifies the expectation of a plane-wave propagation and confirms us to start with a wave equation. In equation A.1.1 $Z_0 = 377\,\Omega$ is the vacuum impedance and $c$ represents the speed of light. We are able to rewrite the wave equation into an integral equation with a Green's function approach which takes reflections at the air-substrate interface into account. If the phase factors in the Green's approach are one and the electric field is constant inside the thin-film stack, the Green's function becomes independent of the propagation direction $z$ and reads approximately as $G_0 \approx (c/i\omega)/(n_1 + n_2)$ [Sei16].

## A.2. THz transmission model

Here, we derive the THz transmission model from scratch. The model bases on measurements of the transmitted THz electric field through the thin-film sample and through a reference such as the substrate without thin film stack. The transmitted electric fields (see Fig. 2.9) can be written as:

$$
\begin{aligned}
E_{\text{ref}} &= 2ik_1 \cdot G_{\text{ref}} \cdot E_{\text{in}} & \text{(A.2.1)} \\
&= t_{12} \cdot E_{\text{in}} & \text{(A.2.2)} \\
E_{\text{sample}} &= \frac{2ik_1 \cdot E_{\text{in}}}{G_{\text{ref}}^{-1} + \int \mathrm{d}z \Delta(k^2)} & \text{(A.2.3)}
\end{aligned}
$$

with the Green's function $G_{\text{ref}} = \frac{1}{i(k_1+k_2)}$ and $\Delta(k^2) = k^2(z) - k_2^2$. Calculating the ratio of $E_{\text{ref}}$ and $E_{\text{sample}}$, we yield

$$\frac{E_{\text{sample}}}{E_{\text{ref}}} = \frac{1}{1 + G_{\text{ref}} \int \mathrm{d}z \Delta(k^2)} \tag{A.2.4}$$

We note that for arbitrary angles of incidence $\theta$ the wave vector $k^2(z)$ depends on $\theta$.

$$k^2(z) = \left(\frac{\omega}{c} n(z)\right)^2 - k_\parallel = \left(\frac{\omega}{c} n(z)\right)^2 - \frac{\omega}{c} \cdot \sin(\theta) \tag{A.2.5}$$

If $\theta = 0°$, the expression $\Delta(k^2)$ simplifies to

$$
\begin{aligned}
\Delta(k^2) &= k^2(z) - k_2^2 & \text{(A.2.6)} \\
&= \frac{\omega^2}{c^2}\left(n^2(z) - n_2^2\right) & \text{(A.2.7)} \\
&= \frac{\omega^2}{c^2}\left(\varepsilon - \varepsilon_2\right) & \text{(A.2.8)}
\end{aligned}
$$

The refractive index $n_2$ is equal to one ($n_2 = 1$) because the medium in the half-space two is air. This leads directly to $\varepsilon_2 = 1$. Now, we compare $\Delta(k^2)$ to the known relation

$$
\Delta(k^2) = \frac{\omega^2}{c^2}\left(\varepsilon - 1\right) \qquad \Leftrightarrow \qquad Z_0\sigma = -i\frac{\omega}{c}\cdot(\varepsilon - 1) \qquad \text{(A.2.9)}
$$

Let's rewrite $\Delta(k^2)$

$$
\Delta(k^2) = -\frac{\omega}{c}\cdot\frac{Z_0\sigma}{i} \qquad \text{(A.2.10)}
$$

This yields an expression for the ratio of sample and reference measurement:

$$
\frac{E_{\text{sample}}(\omega)}{E_{\text{ref}}(\omega)} = \frac{1}{1 + \frac{Z_0}{n_1+1}\int_0^d \mathrm{d}z'\,\sigma(z',\omega)}. \qquad \text{(A.2.11)}
$$

## A.3. TaAu series: additional measurements

Here, we give additionally some more information on the TaAu series measured by Satya Prakash Bommanaboyena from the university of Bielefeld. By measuring the resistances with the four-point method (see section 3.2.2), a difference between 40 nm thick and 3 nm thin-film TaAu layers gets visible (Fig. A.1a).

The thin-film TaAu layers (orange), studied in this thesis, have a much higher resistivity in the Au rich regime due to an island growth of Au on $SiO_x$. Equivalent


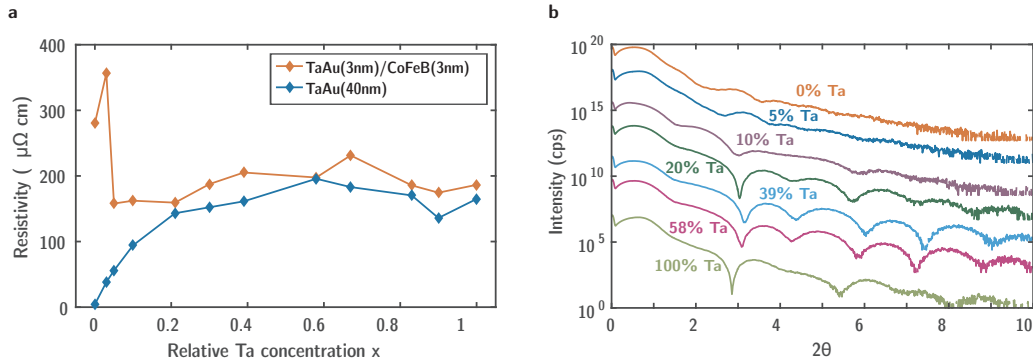
Figure A.1.: **Resistivity and XRR measurements from Ta$_x$Au$_{1-x}$.** **a**, Resistivity measurements show, that the thin-films exhibit a much higher resistivity in the Au rich regime compared to equivalent samples with 40 nm thickness. **b**, XRR measurements revealed that indeed the TaAu layer becomes rough in the Au rich regime.

TaAu samples with a thickness of 40 nm (blue) do not exhibit high resistivities in this regime.

To proof the hypothesis of a rough interface between TaAu and CoFeB, x-ray reflectivity (XRR) measurements were done. XRR is a surface sensitive method, in which x-rays are incident under small angles and get reflected. The intensity of the reflected radiation differs with respect to the surface quality. Detailed information about the XRR method can be found in [Dai09].

Indeed, XRR measurements reveal that the TaAu|CoFeB interface is much rougher in the Au rich regime compared to the Ta rich samples (see Fig. A.1b). Furthermore, the TaAu thin-films gets smoother with increasing Ta concentration.

# Bibliography

[An12]  Z. An, F. Q. Liu, Y. Lin, & C. Liu. *The universal definition of spin current.* Sci. Rep. **2**, 1-6 (2012).

[Ash76]  N. W. Ashcroft, N. D. Mermin. *Solid State Physics.* Brooks/Cole Cengage Learning, 1976.

[Bad90]  J. Badoz, M. P. Silverman & J. C. Canit. *Wave propagation through a medium with static and dynamic birefringence: theory of the photoelastic modulator.* J. Opt. Soc. Am. A. **7**, 672 (1990).

[Bau12]  G. E. W. Bauer, E. Saitoh, & B. J. van Wees. *Spin caloritronics.* Nat. Mater. **11**, 391-399 (2012).

[Ber17]  A. J. Berger, E. R. J. Edwards, H. T. Nembach, A. D. Karenowska, M. Weiler, & T. J. Silva. *Inductive detection of field-like and damping-like AC inverse spin-orbit torques in ferromagnet/normal metal bilayers.* ArXiv, 1611.05798v2 (2017).

[Boy08]  R. W. Boyd. *Nonlinear Optics.* 3rd ed., Elsevier Acad. Press, Amsterdam, 2008.

[Bra16a]  L. Braun, G. Mussler, A. Hruban, M. Konczykowski, T. Schumann, M. Wolf, M. Münzenberg, L. Perfetti, & T. Kampfrath. *Ultrafast photocurrents at the surface of the three-dimensional topological insulator $Bi_2Se_3$.* Nat. Commun. **7**, 13259 (2016).

[Bra16b]  L. Braun. *Electron and Phonon Dynamics in Topological Insulators at THz Frequencies.* Dissertation, Freie Universiät Berlin (2016).

[Brü12]  E. Bründermann, H.-W. Hübers, & M. FitzGerald Kimmitt. *Terahertz Techniques.* Springer Series in Optical Science, Bd. 151, Heidelberg, 2012.

[Cha15]  K. Chadova, S. Wimmer, H. Ebert, & D. Ködderitzsch. *Tailoring of the extrinsic spin Hall effect in disordered metal alloys.* Phys. Rev. B **92**, 235142 (2015).

[Cha16]  C.-Z. Chang, & M. Li. *Quantum anomalous hall effect in time-reversal-symmetry breaking topological insulators.* J. Phys. Condens. Matter **28**, 123002 (2016).

[Cha07]  C. Chappert, A. Fert, & F. Nguyen van Dau. *The emergence of spin electronics in data storage.* Nat. Mater. **6**, 813-823 (2007).

[Che17] T.-Y. Chen, C.-T. Wu, H.-W. Yen, & C.-F. Pai. *Tunable spin-orbit torque in Cu-Ta binary alloy heterostructures*. Phys. Rev. B **96**, 1-7 (2017).

[Chu07] E. M. Chudnovsky. *Theory of the Spin Hall Effect: Extension of the Drude Model*. Phys. Rev. Lett. **99**, 206601 (2007).

[Coe02] R. Coehoorn. *Novel Magnetoelectronic Materials and Devices - Electrical conduction in magnetic metals Spin-flip processes Spin-polarized transport in CPP devices*. Lecture Notes, Eindhoven University of Technology (2002).

[Cra17] J. Cramer, T. Seifert, A. Kronenberg, F. Fuhrmann, G. Jakob, M. Jourdan, T. Kampfrath, & M. Kläui. *Complex THz and DC inverse spin Hall effect in $YIG/Cu_{1-x}Ir_x$ bilayers across a wide concentration range*. ArXiv, 1709.01890 (2017).

[Dai09] J. Daillant, & A. Gibaud. *X-ray and Neutron Reflectivity. Principles and Applications*. Springer, Heidelberg, 2009.

[Dem13] W. Demtröder. *Experimentalphysik 2: Elektrizität und Optik*. 6. Auflage, Springer Spektrum, Heidelberg, 2013.

[Dem16] K.-U. Demasius, T. Phung, W. Zhang, B. P. Hughes, S.-H. Yang, A. Kellock, W. Han, S. S.P. Parkin. *Enhanced spin-orbit torques by oxygen incorporation in tungsten film*. Nat. Commun. **7**, 10644 (2016).

[Dex08] S. L. Dexheimer. *Terahertz Spectroscopy: Principles and Applications*. CRC press, 2007.

[Dhe67] P. N. Dheer. *Galvanomagnetic Effects in Iron Whiskers*. Physical Review **156**, 637-644 (1967).

[Dhi17] S. S. Dhillon, M. S. Vitiello, E. H. Linfield, A. G. Davies, M. C. Hoffmann, J. Booske, C. Paoloni, M. Gensch, P. Weightman, G. P. Williams, E. Castro-Camus, D. R. S. Cumming, F. Simoens, I. Escorcia-Carranza, J. Grant, S. Lucyszyn, M. Kuwata-Gonokami, K. Konishi, M. Koch, C. A. Schmuttenmaer, T. L. Cocker, R. Huber, A. G. Markelz, Z. D. Taylor, V. P. Wallace, J. A. Zeitler, J. Sibik, T. M. Korter, B. Ellison, S. Rea, P. Goldsmith, K. B. Cooper, R. Appleby, D. Pardo, P. G. Huggard, V. Krozer, H. Shams, M. Fice, C. Renaud, A. Seeds, A. Stöhr, M. Naftaly, N. Ridler, R. Clarke, J. E. Cunningham, & M. B. Johnston. *The 2017 terahertz science and technology roadmap*. J. Phys. D. Appl. Phys. **50**, (2016).

[Ebe17] H. Ebert. *SPRKKR. A spin polarized relativistic Korringa-Kohn-Rostoker (SPR-KKR) code for Calculating Solid State Properties*. User's Guide, version 7.7 (05.12.2017), Universität München (2017).

[Eic10]  J. Eichler, H.J. Eichler. *Laser: Bauformen, Strahlführung, Anwendungen.* 7. Auflage, Springer-Verlag, Heidelberg, 2010.

[Hai17]  T. Haider. *A Review of Magneto-Optic Effects and Its Application.* Int. J. Electromagn. Appl. **7**, 17-24 (2017).

[Hay14]  M. Hayashi, J. Kim, M. Yamanouchi, & H. Ohno. *Quantitative characterization of the spin-orbit torque using harmonic Hall voltage measurements.* Phys. Rev. B. - Condens. Matter Mater. Phys. **89**, 1-15 (2014).

[Hui17]  T. J. Huisman, R. V. Mikhaylovskiy, T. Rasing, & A. V. Kimel. *Sub-100-ps dynamics of the anomalous Hall effect at terahertz frequencies.* Phys. Rev. B. **95**, 1-8 (2017).

[Hwa15]  H. Y. Hwang, S. Fleischer, N. C. Brandt, B. G. Perkins Jr., M. Liu, K. Fan, A. Sternbach, X. Zhang, R. D. Averitt & K. A. Nelson. *A review of non-linear terahertz spectroscopy with ultrashort tabletop-laser pulses.* J. Mod. Opt. **62**, 1447-1479 (2015).

[Jin15]  Z. Jin, A. Tkach, F. Casper, V. Spetter, H. Grimm, A. Thomas, T. Kampfrath, M. Bonn, M. Kläui, & D. Turchinovich. *Accessing the fundamentals of magnetotransport in metals with terahertz probes.* Nat. Phys. **11**, 761-766 (2015).

[Kaj10]  Y. Kajiwara, K. Harii, S. Takahashi, J. Ohe, K. Uchida, M. Mizuguchi, H. Umezawa, H. Kawai, K. Ando, K. Takanashi, S. Maekawa & E. Saitoh. *Transmission of electrical signals by spin-wave interconversion in a magnetic insulator.* Nature **464**, 262-266 (2010).

[Kam13a]  T. Kampfrath, M. Battiato, P. Maldonado, G. Eilers, J. Nötzold, S. Mährlein, V. Zbarsky, F. Freimuth, Y. Mokrousov, S. Blügel, M. Wolf, I. Radu, P. M. Oppeneer, & M. Münzenberg. *Terahertz spin current pulses controlled by magnetic heterostructures.* Nat. Nanotech. **8**, 256 (2013).

[Kam13b]  T. Kampfrath, K. Tanaka, & K. A. Nelson. *Resonant and nonresonant control over matter and light by intense terahertz transients.* Nat. Photonics **7**, 680-690 (2013).

[Kar54]  R. Karplus, & J. M. Luttinger. *Hall Effect in Ferromagnetics.* Phys. Rev. **95**, 1154-1160 (1954).

[Kre18]  K. L. Krewer, Z Mics, J Arabski, G. Schmerber, E. Beaurepaire, M Bonn, & D Turchinovich. *Accurate terahertz spectroscopy of supported thin films by precise substrate thickness correction.* Opt. Lett. **43**, 447-450 (2018).

[Lac14]  P. Laczkowski, J.-C. Rojas-Sánchez, W. Savero-Torres, H. Jaffrès, N. Reyren, C. Deranlot, L. Notin, C. Beigné, A. Marty, J.-P. Attané, L. Vila, J.-M. George, & A. Fert. *Experimental evidences of a large extrinsic spin Hall effect in AuW alloy.* Appl. Phys. Lett. **104**, 142403 (2014).

[Lac17]  P. Laczkowski, Y. Fu, H. Yang, J.-C. Rojas-Sánchez, P. Noel, V.T. Pham, G. Zahnd, C. Deranlot, S. Collin, C. Bouard, P. Warin, V. Maurel, M. Chshiev, A. Marty, J.-P. Attané, A. Fert, H. Jaffrès, L. Vila, & J.-M. George. *Large enhancement of the spin Hall effect in Au by scattering with side-jump on Ta impurities.* Phys. Rev. B **96**, 140405(R), 1-5 (2017).

[Lei99]  A. Leitenstorfer, S. Hunsche, J. Shah, M.C. Nuss, & W.H. Knox. *Femtosecond Charge Transport in Polar Semiconductors.* Phys. Rev. Lett. **82**, 5140-5143 (1999).

[Lie17]  L. Liensberger. *Spin-Orbit Torques and Magnetization Dynamics in Non-collinear Magnets.* Master Thesis, Technische Universität München (2017).

[Miy07]  T. Miyasato, N. Abe, T. Fujii, A. Asamitsu, S. Onoda, Y. Onose, N. Nagaosa, & Y. Tokura. *Crossover Behavior of the Anomalous Hall Effect and Anomalous Nernst Effect in Itinerant Ferromagnets.* Phys. Rev. Lett. **99**, 1-4 (2007).

[Mon17]  S. Monda, S. Choudhury, N. Jha, A. Ganguly, J. Sinha, & A. Barman. *All-optical detection of the spin Hall angle in W/CoFeB/SiO$_2$ heterostructures with varying thickness of the tungsten layer.* Phys. Rev. B **96**, 1-8 (2017).

[Nag10]  N. Nagaosa, J. Sinova, s. Onoda, A. MacDonald, & N. Ong. *Anomalous hall effect.* Rev. Mod. Phys. **82**, 1539-1592 (2010).

[Ngu16]  M.-H. Nguyen, M. Zhao, D. C. Ralph, & R. A. Buhrman. *Enhanced spin Hall torque efficiency in Pt$_{100-x}$Al$_x$ and Pt$_{100-x}$Hf$_x$ alloys arising from the intrinsic spin Hall effect.* Appl. Phys. Lett. **108**, 242407 (2016).

[Nol15]  W. Nolting. *Grundkurs Theoretische Physik 5/2: Quantenmechanik - Methoden und Anwendungen.* 8. Auflage, Springer Spektrum, Heidelberg (2015).

[Obs16]  M. Obstbaum, M. Decker, A. K. Greitner, M. Haertinger, T. N. G. Meier, M. Kronseder, K. Chadova, S. Wimmer, D. Ködderitzsch, H. Ebert, & C. H. Back. *Tuning Spin Hall Angles by Alloying.* Phys. Rev. Lett. **117**, 1-5 (2016).

[Ohr02]  M. Ohring. *Materials Science of Thin Films: Deposition and Structure.* Adademic Press, San Diego (2002).

[Ong08]  N. P. Ong. *Recipe for spin currents.* Nature **455**, 1741-743 (2008).

[Pra17] S. Prakash Bommanaboyena. *Investigation of Large Spin Hall Angle Materials for THz Emission and Spin-Orbit Torque switching.* Master Thesis, Technische Universität Darmstadt (2017).

[Pri15] S. Priyadarshi, K. Pierz, & M. Bieler. *Detection of the Anomalous Velocity with Subpicosecond Time Resolution in Semiconductor Nanostructures.* Phys. Rev. Lett. **115**, 1-6 (2015).

[Qu18] D. Qu, S. Y. Huang, G. Y. Guo, & C. L. Chien. *Inverse spin Hall effect in $Au_x Ta_{1-x}$ alloy film.* Phys. Rev. B **97**, 24402 (2018).

[Ram17] R. Ramaswamy, Y. Wang, M. Elyasi, M. Motapothula, T. Venkatesan, X. Qiu, & H. Yang. *Extrinsic Spin Hall Effect in $Cu_{1-x}Pt_x$.* Phys. Rev. Appl. **8**, 1-8 (2017).

[Rul05] C. Rullière. *Femtosecond laser pulses: Principles and experiments.* 2nd ed., Springer, New York (2005).

[Saj17] M. Sajadi, M. Wolf, & T. Kampfrath. *Transient birefringence of liquids induced by terahertz electric-field torque on permanent molecular dipoles.* Nat. Comm. **8**, 1-8 (2017).

[Sch05] G. Schmidt. *Transient birefringence of liquids induced by terahertz electric-field torque on permanent molecular dipoles.* J. Phys. D. Appl. Phys. **38**, R107-R122 (2005).

[Sei13] T. Seifert. *Generation of Intense and Spectrally Narrow Terahertz Pulses.* Master Thesis, Freie Universität Berlin (2013).

[Sei16] T. Seifert, S. Jaiswal, U. Martens, J. Hannegan, L. Braun, P .Maldonado, F. Freimuth, A. Kronenberg, J. Henrizi, I. Radu, E. Beaurepaire, Y. Mokrousov, P. M. Oppeneer, M. Jourdan, G. Jakob, D. Turchinovich, L. M. Hayden, M. Wolf, M. Münzenberg, M. Kläui, & T. Kampfrath. *Efficient metallic spintronic emitters of ultrabroadband terahertz radiation.* Nat. Photonics **10**, 483-488 (2016).

[Sei17a] T. Seifert, S. Jaiswal, M. Sajadi, G. Jakob, S. Winnerl, M. Wolf, M. Kläui, & T. Kampfrath. *Ultrabroadband single-cycle terahertz pulses with peak fields of 300 kV $cm^{-1}$ from a metallic spintronic emitter.* Appl. Phys. Lett. **110** (2017).

[Sei17b] T. Seifert, S. Jaiswal, J. Barker, I. Razdolski, J. Cramer, O. Gueckstock, S. Maehrlein, L. Nadvornik, S. Watanabe, C. Ciccarelli, A. Melnikov, G. Jakob, M. Münzenberg, S.T.B. Goennenwein, G. Woltersdorf, P.W. Brouwer, M. Wolf, M. Kläui, & T. Kampfrath. *Launching magnons at terahertz speed with the spin Seebeck effect.* ArXiv, 1709.00768 (2017).

[Sei17c] T. Seifert. *Spintronics with Terahertz Radiation: Probing and driving spins at highest frequencies.* Dissertation, Freie Universität Berlin (2017).

[Sin15]  J. Sinova, S. O. Valenzuela, J. Wunderlich, C. Back, & T. Jungwirth. *Spin hall effects.* Rev. Mod. Phys. **87**, 1213-1260 (2015).

[Sun05]  Q.-f. Sun & X. Xie. *Definition of the spin current: The angular spin current and its physical consequences.* Phys. Rev. B **72**, 245305 (2005).

[Sug00]  S. Sugano, N. Kojima. *Magneto-Optics.* Springer series in solid-state sciences Vol. 128, Springer, Berlin (2000).

[Sto06]  J. Stöhr, H. C. Siegmann. *Magnetism: From Fundamentals to Nanoscale Dynamics.* Springer series in solid-state sciences Vol. 152, Springer, Berlin (2006).

[Sve15]  V. Sverdlov, & S. Selberherr. *Silicon spintronics: Progress and challenges.* Phys. Rep. **585**, 1-40 (2015).

[Tan08]  C. Tannous, J. Gieraltowski. *A Stoner-Wohlfarth model Redux: Static properties.* Phys. B Condens. Matter **403**, 3563-3570 (2008).

[Tom13]  A. Tomasino, A. Parisi, S. Stivala, P. Livreri, A. C. Cino, A. C. Busacca, M. Peccianti & R. Morandotti. *Wideband THz Time Domain Spectroscopy based on Optical Rectification and Electro-Optic Sampling.* Sci. Rep. **3**, 3116 (2013).

[Uch08]  K. Uchida, S. Takahashi, K. Harii, J. Ieda, W. Koshibae, K. Ando, S. Maekawa, & E. Saitoh. *Observation of the spin Seebeck effect.* Nature **455**, 778-781 (2008).

[Uch12]  K. Uchida, T. Ota, H. Adachi, J. Xiao, T. Nonaka, Y. Kajiwara, G. E. W. Bauer, S. Maekawa, & E. Saitoh. *Thermal spin pumping and magnon-phonon-mediated spin-Seebeck effect K..* J. Appl. Phys. **111**, 103903 (2012).

[Wal16]  J. Walowski & M. Münzenberg. *Perspective: Ultrafast magnetism and THz spintronics.* J. Appl. Phys. **120**, (2016).

[Wei11]  J. Weischenberg, F. Freimuth, J. Sinova, S. Blügel, & Y. Mokrousov. *Ab Initio Theory of the Scattering-Independent Anomalous Hall Effect.* Phys. Rev. Lett. **107**, 1-5 (2011).

[Wei14]  D. Wei, M. Obstbaum, M. Ribow, C. H. Back. & G. Woltersdorf. *Spin Hall voltages from a.c. and d.c. spin currents.* Nat. Commun. **5**, 1-6 (2014).

[Wen17]  Y. Wen, J. Wu, P. Li, Q. Zhang, Y. Zhao, A. Manchon, J. Q. Xiao, & X Zhang. *Temperature dependence of spin-orbit torques in Cu-Au alloys.* Phys. Rev. B **95**, 1-8 (2017).

[Whi72]  R. M. White. *Quantum theory of magnetism: Magnetic Properties of Materials.* 3rd ed., Springer, New York, 1972.

[Wol01]  S. A. Wolf, D. D. Awschalom, R. A. Buhrman, J. M. Daughton, S. von Molnár, M. L. Roukes, A. Y. Chtchelkanova & D. M. Treger. *Spintronics: A Spin-Based Electronics Vision for the Future*. Science **294**, 1488 (2001).

[Wu16]  H. Wu, C. Fang, Z. Yuan, X. F. Han, & C. H. Wan. *Spin seebeck and spin-dependent seebeck effect in ferromagnetic thin films*. IEEE International Nanoelectronics Conference (INEC), 1-2, Chengdu (2016).

[Xu16]  Y. Xu, D. D. Awschalom, J. Nitta. *Handbook of Spintronics*. Springer Science+Business Media, Dordrecht (2016).

[Zhu06]  V. P. Zhukov, E. V. Chulkov, & P. M. Echenique. *Lifetimes and inelastic mean free path of low-energy excited electrons in Fe, Ni, Pt, and Au: Ab initio GW+T calculations*. Phys. Rev. B **73**, 125105 (2006).

[Zou16]  L. K. Zou, S. H.Wang, Y. Zhang, J. R. Sun, J.W. Cai, & S. S. Kang. *Large extrinsic spin Hall effect in Au-Cu alloys by extensive atomic disorder scattering*. Phys. Rev. B **93**, 1-6 (2016).

# Acknowledgments

I wish to thank Prof. Dr. Stefan Eisebitt for being my primary and official supervisor. Equally I wish to thank Prof. Dr. Martin Wolf from the Fritz-Haber-Institute of the Max-Planck-Society for the second expertise of my thesis.

I thank cordially Prof. Dr. Tobias Kampfrath for the possibility to write this thesis in his group "Terahertz Physics" located at the Fritz-Haber-Institute (FHI) and all of his useful advises during the last year.

I wish to thank Tom Seifert for introducing me to the experimental setup and being my daily supervisor. Without his good idea and patient help in the lab as well as his hints during the evaluation of the data, this thesis wouldn't be possible.
I thank Seyed Mohammadreza Rouzegar for simulating the electromagnet with COM-SOL. In addition, I wish to thank all members of the Terahertz Physics Group Dr. Lukas Braun, Julius Heitz, Dr. Sebastian Mährlein, Patrick Müller, Dr. Lukáš Nádvorník and Dr. Mohsen Sajadi for their helpful support during the last twelve months. You are the best!

Furthermore, I want to thank Thomas Zehentbauer for his help concerning all electronical issues and the prototype of the electromagnet, and Reinhard Franke for solving all mechanical problems on incredible short time scales.

At last, I wish to thank the people, who were producing all the samples, measured in this thesis: Prof. Dr. Markus Meinert from the university of Bielefeld and his group members Satya Prakash Bommanaboyena, Sebastian Dapper and Björn Gliniors for the $\beta$-tungsten, tantalum-gold and gold-platinum samples, as well as for the harmonic Hall measurements. I want to thank Mathias Kläui and his team from the university of Mainz for the CoFeB|Pt samples. In addition, I wish to thank Dr. Mathias Weiler and Lukas Liensberger from the Walther-Meißner-Institute in Garching for the VNA-FMR measurements in the GHz range. And I thank Sebastian Wimmer from the LMU Munich for the ab-initio calculations of the TaAu series.